Icarus 335 (2020) 113419

Contents lists available at ScienceDirect

Icarus

journal homepage: www.elsevier.com/locate/icarus

The environmental effects of very large bolide impacts on early Mars explored with a hierarchy of numerical models

Martin Turbet[a,*], Cedric Gillmann[b,c], Francois Forget[a], Baptiste Baudin[a,d], Ashley Palumbo[e], James Head[e], Ozgur Karatekin[b]

[a] Laboratoire de Météorologie Dynamique/IPSL, CNRS, Sorbonne Université, Ecole normale supérieure, PSL Research University, Ecole Polytechnique, Paris 75005, France
[b] Royal Observatory of Belgium, Brussels, Belgium
[c] Free University of Brussels, Department of Geosciences, G-Time, Brussels, Belgium
[d] Magistère de Physique Fondamentale, Département de Physique, Univ. Paris-Sud, Université Paris-Saclay, Orsay Campus, Orsay 91405, France
[e] Department of Earth, Environmental, and Planetary Sciences, Brown University, Providence, RI 02912, USA

A B S T R A C T

The origin of the presence of geological and mineralogical evidence that liquid water flowed on the surface of early Mars is now a 50-year-old mystery. It has been proposed (Segura et al., 2002, 2008, 2012) that bolide impacts could have triggered a long-term climate change, producing precipitation and runoff that may have altered the surface of Mars in a way that could explain (at least part of) this evidence. Here we use a hierarchy of numerical models (a 3-D Global Climate Model, a 1-D radiative-convective model and a 2-D Mantle Dynamics model) to test that hypothesis and more generally explore the environmental effects of very large bolide impacts ($D_{impactor} > 100$ km, or $D_{crater} > 600$ km) on the atmosphere, surface and interior of early Mars.

Using a combination of 1-D and 3-D climate simulations, we show that the environmental effects of the largest impact events recorded on Mars are characterized by: (i) a short impact-induced warm period (several tens of Earth years for the surface and atmosphere to be back to ambient conditions after very large impact events); (ii) a low amount of hydrological cycling of water (because the evaporation of precipitation that reached the ground is extremely limited). The total cumulative amount of precipitation (rainfall) can be reasonably well approximated by the initial post-impact atmospheric reservoir of water vapour (coming from the impactor, the impacted terrain and from the sublimation of permanent ice reservoirs heated by the hot ejecta layer); (iii) deluge-style precipitation (~2.6 m Global Equivalent Layer of surface precipitation per Earth year for our reference simulation, quantitatively in agreement with previous 1-D cloud free climate calculations of Segura et al., 2002), and (iv) precipitation patterns that are uncorrelated with the observed regions of valley networks.

However, we show that the impact-induced stable runaway greenhouse state predicted by Segura et al. (2012) should not be achievable if convection and water vapour condensation processes are considered. We nevertheless confirm the results of Segura et al. (2008) and Urata and Toon (2013) that water ice clouds could in theory significantly extend the duration of the post-impact warm period, and even for cloud coverage significantly lower than predicted in Ramirez and Kasting (2017). However, the range of cloud microphysical properties for which this scenario works is very narrow.

Using 2-D Mantle Dynamics simulations we find that large bolide impacts can produce a strong thermal anomaly in the mantle of Mars that can survive and propagate for tens of millions of years. This thermal anomaly could raise the near-surface internal heat flux up to several hundreds of mW/m^2 (i.e. up to ~10 times the ambient flux) for several millions years at the edges of the impact crater. However, such internal heat flux is largely insufficient to keep the martian surface above the melting point of water.

In addition to the poor temporal correlation between the formation of the largest basins and valley networks (Fassett and Head, 2011), these arguments indicate that the largest impact events are unlikely to be the direct cause of formation of the Noachian valley networks. Our numerical results support instead the prediction of Palumbo and Head (2018) that very large impact-induced rainfall could have caused degradation of large craters, erased small craters, and formed smooth plains, potentially erasing much of the previously visible morphological surface history. Such hot rainfalls may have also led to the formation of aqueous alteration products on Noachian-aged terrains, which is consistent with the timing of formation of clays.

1. Introduction

Since the 1970s, scientists have discovered an overwhelming number of pieces of evidence that liquid water flowed on ancient Mars: high erosion rates (Craddock and Howard, 2002; Mangold et al., 2012; Quantin-Nataf et al., 2019), sedimentary deposits (Grotzinger et al., 2015; Williams et al., 2013), hydrated minerals (Bibring et al., 2006; Carter et al., 2015, 2013; Ehlmann et al., 2011; Mustard et al., 2008; Poulet et al., 2005) and dry river beds and lakes (Cabrol and Grin, 1999; Carr, 1995; Hynek et al., 2010; Malin and Edgett, 2003; Mangold and Ansan, 2006; Moore et al., 2003). Sophisticated climate modeling under ancient Mars conditions assuming a faint young Sun and $CO_2/N_2/H_2O$

* Corresponding author.
E-mail address: mturbet@lmd.jussieu.fr (M. Turbet).

https://doi.org/10.1016/j.icarus.2019.113419
Received 20 February 2019; Received in revised form 26 July 2019; Accepted 22 August 2019
Available online 31 August 2019
0019-1035/

atmospheres have not yet been able to produce liquid water or significant precipitation anywhere on the red planet (Forget et al., 2013; Wordsworth et al., 2013), unless additional hypothetic greenhouse gases were incorporated, such as reducing gases CH_4 or H_2 (Kite et al., 2017; Ramirez and Kaltenegger, 2017; Ramirez and Kaltenegger, 2018; Ramirez et al., 2014a; Turbet et al., 2019; Wordsworth et al., 2017).

It has been suggested that the warmer and wetter (compared to present-day Mars) conditions required to explain the formation of the aforementioned geological and mineralogical evidence could have been produced in response to impact-induced climate change (Haberle et al., 2017; Segura et al., 2008, 2002; Steakley et al., 2018; Toon et al., 2010; Turbet, 2018; Wordsworth et al., 2013; Wordsworth, 2016).

The environmental effects of such bolide impact events have already been studied with unidimensional radiative-convective models (Segura et al., 2012, 2008, 2002). Here we improve upon this previous work by exploring the climatic impact of very large bolide impact events using a hierarchy of numerical models, ranging from (i) a 3-D Global Climate Model to (ii) a 1-D radiative-convective model and ultimately to (iii) a 2-D mantle dynamics numerical code. The 3-D Global Climate Model (GCM) simulations are used to accurately simulate all the processes (cloud microphysics, large scale circulation, etc.) at play in the post-impact early martian atmosphere. 1-D radiative-convective model simulations are used to simulate a wide range of possible post-impact conditions (initial atmosphere, size of impactor, etc.) and explore the sensitivity to parameterizations (e.g. microphysics of clouds), thanks to their low computational cost. Eventually, the 2-D mantle dynamics numerical code is used to explore the long-term effects of large bolide impacts on the surface and near-surface environment on ancient Mars.

This paper focuses on the environmental effects of the largest impact events ever recorded on Mars, i.e. those that are large enough (impactor diameter typically larger than 100 km, corresponding to a crater diameter roughly larger than 600 km, using Toon et al., 2010 scaling relationship) to typically vaporize the equivalent of the present-day Mars water content (around 34 m Global Equivalent Layer [GEL]; Carr and Head, 2015) in the atmosphere, as estimated from energy conservation calculations. Although the formation of the largest basins visible today on Mars (e.g. Hellas, Argyre, Isidis) is now thought to have occurred earlier in time than the formation of the martian valley networks (Fassett and Head, 2008, 2011; Werner, 2014) (compared to Toon et al., 2010 that used basin age estimates of Werner, 2008), very large impact events must have had a profound impact on the surface of early Mars.

The specific processes that occur following a basin-scale impact event on Mars have been explored by Segura et al. (2008, 2002) and Toon et al. (2010) and revisited from a geological perspective by Palumbo and Head (2018). Before discussing the specific modeling done in this work, we first re-iterate the key processes involved in Impact Cratering Atmospheric and Surface Effects (ICASE) (Palumbo and Head, 2018). When a very large impactor collides with the martian surface, a significant amount of energy is transferred from the impactor to the surface. The intense energy of the impact event will cause all projectile material and some target martian material to be pulverized (and ejected from the crater), melted (forming a melt layer on the crater floor), or vaporized. The vaporized component is of specific interest for this analysis. The vaporized material expands and moves away from the crater, producing an extremely hot plume consisting of target and projectile material. The specific constituents of the plume include water vapour and vaporized silicate material. For large, energetic impact events such as the ones explored in the present work, the plume will expand globally. Atmospheric temperatures are expected to be very hot, above the condensation temperature of both the silicate material and water. The atmosphere begins cooling from the initial extremely hot state and, due to the differences in condensation temperature, the silicate material is expected to condense and fall out of the atmosphere before the water vapour. Upon condensation, the silicate material is expected to fall out of the atmosphere and distribute globally, forming something similar to a very hot terrestrial spherule layer. The high temperature of this silicate-debris layer will cause any remaining underlying water ice to vaporize and enter the atmosphere. At this point, we expect that the entire initial surface water inventory would be as vapour in the atmosphere. Based on this description of the post-impact effects that occur following a basin-scale impact event on Mars (following Palumbo and Head, 2018), we set out to constrain the duration and characteristics of impact-induced rainfall using a hierarchy of numerical models. Specifically, we explore two main aspects of post-impact effects in this manuscript:

1. How long can the surface of Mars be kept above the melting point of water following large bolide impact events? In particular, can an impact-induced, stable runaway climate exist on early Mars, as previously reported by Segura et al. (2012)? Can impact-induced, high altitude water ice clouds keep the surface of Mars above the melting point of water for extended periods of time, as previously reported by Segura et al. (2008) and Urata and Toon (2013)?
2. How much precipitation is generated after large bolide impacts events, and how is it distributed across the surface of Mars?

A major, original aspect of our work is to explore how 3-dimensional processes (atmospheric circulation and cloud formation) affect the environmental effects of bolide impact events.

We first describe the various numerical models used in this work in Section 2: (i) The 3-D LMD Generic Global Climate Model, (ii) the 1-D LMD Generic inverse radiative-convective model and (iii) the StagYY 2-D mantle dynamics code. We then present in Section 3 the results of our 3-D global climate simulations of the environmental effects of large bolide impact events on the atmosphere and surface of early Mars. Because we show that in some conditions 3-D post-impact atmospheres can be remarkably well described by 1-D simulations, we then use our 1-D radiative-convective simulations in Section 4 to explore a wide range of possible impact-induced conditions. Eventually, we use in Section 5 our 2-D mantle dynamics numerical simulations to model the long-term effects of very large impacts on the interior, near-surface and surface of Mars. We revisit throughout the manuscript the results of Segura et al. (2012, 2008, 2002), Urata and Toon (2013) and Ramirez and Kasting (2017).

2. Method

In this section, we describe the hierarchy of numerical models used for the present study. We first describe the two different versions (3-D and 1-D) of the LMD Generic climate model, designed here to reproduce the post-impact conditions following a very large impactor hitting the surface of early Mars. We assume that the planet - initially endowed with a CO_2-dominated atmosphere - is suddenly warmed and moistened following processes described in Palumbo and Head (2018) and summarized in the previous section. We then present the radiative transfer scheme (common for the two models), with a particular focus on the recent improvements made on the spectroscopy of dense CO_2 + H_2O atmospheres (typical of post-impact atmospheres) that are taken into account in the radiative transfer calculations. Eventually, we describe the StagYY 2-D mantle dynamics code used to model the long-term effects of very large impacts on the surface and near-surface of Mars.

2.1. 3-D global climate model simulations

The model described in this subsection was used to produce the results described in Section 3.

Our 3-D LMD Generic model is a full 3-Dimensions Global Climate Model (GCM) that has previously been developed and used for the study of the climate of ancient Mars (Forget et al., 2013; Palumbo et al., 2018; Turbet et al., 2017a; Wordsworth et al., 2013, 2015).

The simulations presented in this paper were performed at a spatial

resolution of 96 × 64 in longitude × latitude (i.e. 3.8° × 2.8°; 220 km × 165 km at the equator). In the vertical direction, the model is composed of 45 distinct atmospheric layers, ranging from the surface up to a few Pascals. Hybrid σ coordinates (where σ is the ratio between pressure and surface pressure) and fixed pressure levels were used in the lower and the upper atmosphere, respectively.

The dynamical time step of the simulations ranged between 9 s (at the beginning of the large impact events) and 90 s. The radiative transfer (described in subsection 2.3) and the physical parameterizations (such as condensation, convection, etc.) are calculated every 10 and 40 dynamical time steps, respectively.

Recent work has suggested that the Tharsis rise may have been largely emplaced after the formation of the valley networks (e.g. Bouley et al., 2016). Thus, at the time of the large basin impact events, which is now thought to have occurred earlier in time than valley network formation (Fassett and Head, 2008, 2011; Werner, 2014), we assume topography that is consistent with pre-Tharsis conditions. Specifically, we used the pre-True Polar Wander (pre-TPW) topography from Bouley et al. (2016). The pre-TPW topography is based on the present-day MOLA (Mars Orbiter Laser Altimeter) Mars surface topography (Smith et al., 1999; Smith et al., 2001), but without Tharsis and all the younger volcanic features. Moreover, the formation of Tharsis should have produced a large True Polar Wander (TPW) event of 20°–25°, which is also taken into account in the pre-TPW topography.

We set the obliquity of Mars at 40° to be roughly consistent with the most statistically likely obliquity (41.8°) for ancient Mars (Laskar et al., 2004). We also set the eccentricity to zero as in Wordsworth et al. (2013).

To account for the thermal conduction in the subsurface, we used a 19-layers thermal diffusion soil model. The mid-layer depths range from $d_0 \sim 0.15$ mm to $d_{19} \sim 80$ m, following the power law $d_n = d_0 \times 2^n$ with n being the corresponding soil level, chosen to take into account both the diurnal and seasonal thermal waves. We assumed the thermal inertia of the regolith I_{ground} to be equal to:

$$I_{ground} = I_{dry} + 7x_{H_2O}, \quad (1)$$

where $I_{dry} = 250\ J\,m^{-2}\,s^{-1/2}\,K^{-1}$ and x_{H_2O} is the soil moisture (in $kg\,m^{-3}$). The soil moisture is calculated in the first meter of the ground only. More information on this parameterization can be found in Turbet (2018) (Chapter 9 and Figure 9.1). The dry regolith thermal inertia is slightly higher than the present-day Mars global mean thermal inertia in order to account for the higher atmospheric pressure (Piqueux and Christensen, 2009). This expression has been derived from the standard parameterization of the ORCHIDEE (Organising Carbon and Hydrology In Dynamic Ecosystems) Earth land model (Wang et al., 2016). Moreover, we arbitrarily fixed the thermal inertia of the ground to a value of $1500\ J\,m^{-2}\,s^{-1/2}\,K^{-1}$, whenever the snow/ice cover exceeds a threshold of $1000\ kg\,m^{-2}$ (i.e. the snow/ice cover thickness locally exceeds 1 m). We assumed that the martian regolith has a maximum water capacity of $150\ kg\,m^{-2}$, based on a simple bucket model widely used in the Earth land community (Manabe, 1969; Schaake et al., 1996; Wood et al., 1992).

Subgrid-scale dynamical processes (turbulent mixing and convection) were parameterized as in Forget et al. (2013) and Wordsworth et al. (2013). The planetary boundary layer was accounted for by the Mellor and Yamada (1982) and Galperin et al. (1988) time-dependent 2.5-level closure scheme, and complemented by a convective adjustment which rapidly mixes the atmosphere in the case of unstable temperature profiles. Moist convection was taken into account following a moist convective adjustment that originally derives from the 'Manabe scheme' (Manabe and Wetherald, 1967; Wordsworth et al., 2013). In the version of our scheme, relative humidity is let free and limited to 100% (supersaturation is not permitted). This scheme was chosen instead of more refined ones because it is: 1. robust for a wide range of pressures; 2. energy-conservative; and 3. it is a physically consistent scheme for exotic (non-Earth-like) situations such as the ones induced by large bolide impact events. In practice, when an atmospheric grid cell reaches 100% saturation and the corresponding atmospheric column has an unstable temperature vertical profile, the moist convective adjustment scheme is performed to get a stable moist adiabatic lapse rate. In our simulations of large impact events, water vapour can become the dominant atmospheric species. Thus, we used a generalized formulation of the moist-adiabiat lapse rate developed by Leconte et al. (2013) (Supplementary Materials) to account for the fact that water vapour can become a main species in our simulations. In our model we also used the numerical scheme proposed by Leconte et al. (2013) (Supplementary Materials) to account for atmospheric mass change after the condensation or the evaporation of gases (water vapour in our case); this numerical scheme is crucial in our simulations of impact events to model accurately the evolution of the surface pressure and the relative content of CO_2 and H_2O. More details on the scheme can be found in Leconte et al. (2013) (Supplementary Materials).

Both CO_2 and H_2O cycles are included in the GCM used in this work. In our model, CO_2 can condense to form CO_2 ice clouds and surface frost if the temperature drops below the saturation temperature of CO_2 (at a given CO_2 partial pressure). A self-consistent water cycle is also included in the GCM. In the atmosphere, water vapour can condense into liquid water droplets or water ice particles, depending on the atmospheric temperature and pressure, forming clouds.

The fraction of cloud particles $\alpha_{c,liquid}$ (in %) in liquid phase is given by (Charnay, 2014):

$$\alpha_{c,liquid} = \frac{T - (273.15 - 18)}{18} \quad (2)$$

where T is the atmospheric temperature of the corresponding GCM air cell. Above 0 °C, particles are fully liquid and below −18 °C they are assumed to be fully solid.

We used a fixed number of activated cloud condensation nuclei (CCNs) per unit mass of air N_c to determine the local H_2O cloud particle sizes, based on the amount of condensed material. Following Leconte et al. (2013), we used $N_c = 10^4\ kg^{-1}$ for water ice clouds and $10^6\ kg^{-1}$ for liquid water clouds. These numbers - that give satisfactory results to reproduce the present-day Earth climate (Leconte et al., 2013) - are highly uncertain for post-impact conditions on Mars. On the one hand, impact events would inject a huge number of silicated particles in the atmosphere, potentially serving as CCNs. On the other hand, the huge rate of precipitation recorded in our 3-D simulations would remove efficiently these silicated particles. Eventually, we used $N_c = 10^5\ kg^{-1}$ for CO_2 ice clouds following Forget et al. (2013).

The effective radius r_{eff} of the cloud particles is then given by:

$$r_{eff} = \left(\frac{3q_c}{4\pi\rho_c N_c}\right)^{1/3} \quad (3)$$

where ρ_c is the density of the cloud particles ($1000\ kg\,m^{-3}$ for liquid and $920\ kg\,m^{-3}$ for water ice) and q_c is the mass mixing ratio of cloud particles (in kg per kg of air). The effective radius of the cloud particles is then used to compute both (1) their sedimentation velocity and (2) their radiative properties calculated by Mie scattering (see Madeleine, 2011 for more details) for both liquid and ice cloud particles.

Water precipitation is divided into rainfall and snowfall, depending on the nature (and thus the temperature) of the cloud particles. Rainfall is parameterized using the scheme from Boucher et al. (1995), accounting for the conversion of cloud liquid droplets to raindrops by coalescence with other droplets. Rainfall is considered to be instantaneous (i.e. it goes directly to the surface) but can evaporate while falling through sub-saturated layers. The re-evaporation rate of precipitation E_{precip} (in $kg/m^3/s$) is determined by (Gregory, 1995):

$$E_{precip} = 2 \times 10^{-5}\left(1 - \frac{q_v}{q_{s,v}}\right)\sqrt{F_{precip}} \quad (4)$$

where q_v and $q_{s,v}$ are the water vapour mixing ratios in the air cell and at saturation, respectively. F_{precip} is the precipitation flux (in $kg/m^2/s$).

Re-evaporation of precipitation refers to rain that evaporates in the dry lower atmosphere before it reaches the ground.

Snowfall rate is calculated based on the sedimentation rate of cloud particles in the atmospheric layer. The sedimentation velocity of particles V_{sedim} (in m/s) is assumed to be equal to the terminal velocity that we approximate by a Stokes law:

$$V_{\mathrm{sedim}} = \frac{2\rho_c g {r_{\mathrm{eff}}}^2}{9\eta}(1 + \beta K_n) \quad (5)$$

where η is the viscosity of atmospheric CO_2 ($10^5\,\mathrm{N\,s\,m^{-2}}$) and g the gravity of Mars ($3.72\,\mathrm{m\,s^{-2}}$). $(1 + \beta K_n)$ is a 'slip-flow' correction factor (Rossow, 1978), with β a constant equal to $\frac{4}{3}$ and K_n the Knudsen number that increases with decreasing atmospheric pressure.

While the internal and potential energy of condensates (water clouds, here) is accounted for in our convective moist adjustment scheme (see Leconte et al., 2013 lapse rate formulation), we acknowledge that we did not account for the potential, kinetic and internal energy carried by precipitation and that is dissipated in the atmosphere while falling and on the surface energy budget while reaching the surface. A possible strategy to implement the impact of precipitation on the surface energy budget is discussed in Ding and Pierrehumbert (2016).

At the surface, liquid water and water ice can co-exist. Their contributions are both taken into account in the albedo calculation as in Wordsworth et al. (2013). The stability of liquid water/ice/CO_2 ice at the surface is governed by the balance between radiative, latent and sensible heat fluxes (direct solar insolation, thermal radiation from the surface and the atmosphere, turbulent fluxes) and thermal conduction in the soil. Melting, freezing, condensation, evaporation, and sublimation physical processes are all included in the model as in Wordsworth et al. (2013) and Turbet et al. (2017a).

2.2. 1-D inverse climate model simulations

The model described in this subsection was used to produce the results described in Section 4.

Our 1D LMD Generic inverse[1] model is a single-column inverse radiative-convective climate model following the same approach ('inverse modeling') as Kasting et al. (1984), and using the same parameterizations as Ramirez and Kasting (2017). The atmosphere is decomposed into 200 logarithmically-spaced layers that extend from the ground to the top of the atmosphere arbitrarily fixed at 1 Pa. The atmosphere is separated in three (at most) physical layers constructed as follows. First, we fix the surface temperature to the desired value. The first layer is constructed by integrating a moist (H_2O) adiabat upwards until CO_2 starts to condense. This first layer defines a convective troposphere assumed to be fully saturated. From the altitude where CO_2 starts to condense, we construct the second layer by integrating a moist (CO_2) adiabat upwards until the atmospheric temperature reaches the stratospheric temperature, arbitrarily fixed at 155 K as in Ramirez and Kasting (2017).

Once the thermal profile of the atmosphere is constructed, we compute the radiative transfer (described in subsection 2.3) in both visible and thermal infrared spectral domains, and through the 200 atmospheric layers. From this, we derive (1) the Outgoing Longwave Radiation (OLR) and (2) the planetary albedo, from which we can calculate the Absorbed Solar Radiation (ASR). Top Of Atmosphere (TOA) radiative budget can then be computed using OLR and ASR. The radiative transfer calculations are described in details in subsection 2.3.

Following Ramirez and Kasting (2017), we assumed that the planet is flat and the Sun remains fixed at a zenith angle of 60°. The surface albedo is fixed to 0.216.

[1] The inverse model does not solve for temperature, which is specified. Instead, it solves for the TOA fluxes in shortwave and longwave spectral ranges.

Our model can also take into account the radiative effect of clouds following the same approach as in Ramirez and Kasting (2017). A cloud layer can be placed at any arbitrary height (in any of the 200 atmospheric layers, and in any of the three physical layers previously described). We assume 1 km thick cloud decks as in Ramirez and Kasting (2017). Following Ramirez and Kasting (2017), we compute the optical depth τ_{ice} of the water ice clouds as follows:

$$\tau_{\mathrm{ice}} = \frac{3Q_{\mathrm{eff}} IWC \Delta z}{4 r_{\mathrm{ice}} \rho_{\mathrm{ice}}}, \quad (6)$$

with Q_{eff} the extinction coefficient, IWC the ice water content (in g/m^3), Δz the vertical path length of the cloud layer, arbitrarily fixed to 10^3 m, r_{ice} the effective radius of water ice particles, and ρ_{ice} the volumetric mass of water ice, We used the same Mie optical properties (tabulated values of Q_{eff}) for the cloud particles as in the 3-D Global Climate Model (same radiative properties as used in Wordsworth et al., 2013). We assumed that the IWC scales following Ramirez and Kasting (2017):

$$IWC = 0.88P, \quad (7)$$

with P the atmospheric pressure at the cloud deck level. To explore the sensitivity of the results to the cloud content, we used the 'Relative Ice Water Content' which is a multiplicative factor applied to the IWC (Ramirez and Kasting, 2017). It is equal to 1 unless specified.

2.3. Radiative transfer

Our climate models include a generalized radiative transfer code adapted to any mixture of CO_2 and H_2O gases. Our radiative transfer calculations are performed on 38 spectral bands in the thermal infrared and 36 in the visible domain, using the 'correlated-k' approach (Fu and Liou, 1992) suited for fast calculations. 16 non-regularly spaced grid points were used for the g-space integration, where g is the cumulative distribution function of the absorption for each band.

Absorption caused by the absorption of H_2O and CO_2 in the atmosphere was computed using *kspectrum* (Eymet et al., 2016) to yield high-resolution line-by-line spectra. We used the HITRAN2012 database for the H_2O and CO_2 line intensities and parameters (Rothman et al., 2013). In addition, we incorporated the half-width at half maximum of H_2O lines broadened by CO_2 ($\gamma^{\mathrm{H_2O-CO_2}}$) and CO_2 lines broadened by H_2O ($\gamma^{\mathrm{CO_2-H_2O}}$), as well as the corresponding temperature dependence exponents ($n^{\mathrm{H_2O-CO_2}}$ and $n^{\mathrm{CO_2-H_2O}}$), based on Brown et al. (2007), Gamache et al. (2016), Sung et al. (2009) and Delahaye et al. (2016). More details can be found in Turbet et al. (2017b) and Tran et al. (2018).

Collision-induced absorptions, dimer absorptions and far wing absorptions were also taken into account, whenever data was available. Far wings of CO_2 band lines (both CO_2-CO_2 and CO_2-H_2O) were computed using the χ-factor approach, using experimental data from Perrin and Hartmann (1989), Tran et al. (2011) and Tran et al. (2018). The χ-factor is an empirical correction of the Lorentzian line shape adjusted to laboratory measurements. CO_2-CO_2 collision-induced and dimer absorptions were computed based on Baranov et al. (2004), Gruszka and Borysow (1997), Stefani et al. (2013).

H_2O-H_2O continuum was taken into account using the MT_CKD 3.0 database (Mlawer et al., 2012), from 0 to 20,000 $\mathrm{cm^{-1}}$. MT_CKD databases are available on http://rtweb.aer.com/. H_2O-CO_2 continuum was calculated with the line shape correction functions digitized from Ma and Tipping (1992) (validated experimentally by Tran et al., 2019) using line positions and intensities from the HITRAN2012 database (Rothman et al., 2013), with a cut-off distance at 25 $\mathrm{cm^{-1}}$, and from 0 to 20,000 $\mathrm{cm^{-1}}$. The temperature dependence of the continuum was empirically derived using data digitized from Pollack et al. (1993).

More details on the CIAs, dimer absorptions and far wing absorptions can be found in Turbet et al. (2017b) and Tran et al. (2018).

2.4. 2-D mantle dynamics model simulations

The model described in this subsection was used to produce the results described in Section 5.

We used the StagYY 2-D mantle dynamics code (Tackley, 2008) to simulate the long-term effects of very large impacts on the interior of Mars. Specifically, we used the version of the code from Armann and Tackley (2012) and Gillmann and Tackley (2014), adapted to Mars conditions. Geometry is set to 2-D spherical annulus with a 512 × 64 grid and 2 million advected tracers.

The equations of mass, energy and momentum conservation are solved in the mantle, that is considered anelastic, compressible and to be described by the infinite Prandtl number approximation. Boundary conditions at the top of the mantle are free-slip. Top temperature is set by surface temperature. Bottom temperature decreases with core temperature following Nakagawa and Tackley (2004). Physical properties like density, thermal expansivity, and thermal conductivity are depth dependent and are calculated as described in Tackley (1996). The rheology is temperature- and pressure-dependent diffusion creep. Activation energy and volume are chosen according to Karato and Jung (2003) for dry olivine. Initially, radiogenic elements are uniformly distributed. Radiogenic heating decreases with time and is treated as in Armann and Tackley (2012). The mineral solid-phase transitions in the olivine system and in the pyroxene-garnet system are included as discussed in Xie and Tackley (2004). Other physical, Mars-specific parameters used in the convection simulations are detailed in Keller and Tackley (2009). Here we model only solid state convection of the mantle, in a similar way to what has been used previously in studies of impact heating on Mars (Roberts and Arkani-Hamed, 2014; Roberts et al., 2009). Melting is treated as in other studies using the StagYY code (Armann and Tackley, 2012; Nakagawa and Tackley, 2004; Xie and Tackley, 2004). Only melt located above a certain depth (set to 600 km) is considered to be positively buoyant (Ohtani et al., 1998). We assumed it to instantaneously erupt at the surface (Reese et al., 2007), since its migration can be considered to be fast compared to convection processes. Extracted melt is emplaced at the surface at surface temperature. On the timescales relevant for mantle dynamics evolution, surface conditions are assumed not to vary; simulations have been run for constant surface temperatures from 200 K to 300K, without significant modification of the convection pattern. Full coupling featuring in Gillmann and Tackley (2014) and Gillmann et al. (2016) is not used here. Atmosphere content is tracked to assess volatile degassing and constrain simulations based on present-day observation. Impacts are treated in the same way as in Gillmann et al. (2016). Impacts are assumed to be vertical (head-on) for the sake of mantle dynamics effects modeling. Velocity of the impactor was set to 9 km/s for the reference impact. Reference impact time is 4 Ga before present; alternative simulations with different times have been run (4.2 to 3.8 Ga) without significant change. The projectile is assumed to be an asteroid of density 3000 kg/m^3. Volatile composition can vary widely depending on the type of bolide impactors.

Three effects of impacts are considered: atmospheric erosion, volatile delivery and heat deposition in the mantle. Atmospheric erosion has been calculated from parameterization based on the SOVA hydrocode simulations (Shuvalov, 2009; Shuvalov et al., 2014) and extrapolated for larger bodies when necessary, as described by Gillmann et al. (2016). An upper limit to erosion is set by the tangent plane model (Vickery, 1990). Erosion of the atmosphere is found to be limited to 0.1–1% of the total atmosphere at the time of impact for the range of impactors considered. It has thus a minor effect on the global evolution, especially as it is countered by volatile deposition. This second mechanism primarily depends on projectile volatile content. It is limited by impactor mass loss as ejecta during impact process (Shuvalov, 2009) and by the portion of the projectile avoiding melting (Svetsov and Shuvalov, 2015). For large bolide impactors, most of the volatile constituents (~80%) are delivered to the atmosphere. Effects of the impact on the mantle are treated as in Gillmann et al. (2016). Shock pressure, generated by high energy collisions, followed by adiabatic decompression generates heat, leading to the formation of the so-called thermal anomaly in the mantle. A parameterized law from Monteux et al. (2007) is used to account for heat emplaced in the martian mantle on collision. Accretion of solid material and crater excavation are not considered. We neglect crust vaporization by the impactor. Thermal anomalies are integrated into the StagYY temperature field, produce melting and affect subsequent convection patterns.

3. Exploration of the environmental effects of a very large impactor with a full 3-D global climate model

Here we study the environmental effects of very large impact events on the atmosphere and surface of early Mars, using the 3-D Global Climate Model presented in Section 2.1. Because Global Climate Model simulations are computationally very expensive, we focus in this section on one reference post-impact simulation (computational cost of ~50,000 CPU hours on the French OCCIGEN supercomputer) of a very large impactor hitting the surface of Mars, initially assumed to be endowed with a 1 bar pure CO_2 atmosphere. This value of CO_2 surface atmospheric pressure was arbitrarily chosen, but is roughly consistent with the various mineralogical and isotopic constraints summarized in Kite (2009) (Figure 9). We explore the effect of surface pressure with a computationnally much more efficient 1-D numerical climate model in Section 4. The impactor is assumed to be large enough to trigger the vaporization of ~2 bar (i.e. 54 m GEL) of water into the atmosphere[2]. The atmosphere, surface, and subsurface (down to ~80 m, i.e. the deepest layers in the model) are assumed to be suddenly and uniformly heated up to 500 K[3].

Such extreme post-impact conditions are likely typical of the few most extreme impact events forming the largest basins observed on Mars (Segura et al., 2002; Toon et al., 2010).

3.1. Chronology of the event

Our 3-D simulations indicate that the sequence of events following the very large impact event previously described can be decomposed into four main phases:

Phase I: very hot atmosphere, no precipitation. In this first phase, the atmosphere is too warm for water to condense on the surface. Precipitation (produced in the cooler, upper atmosphere) is re-evaporated (in the lower atmospheric layers). This phase ends when the first droplet of water reaches the ground. The atmosphere is then almost entirely saturated in water vapour, and the atmospheric thermal profile follows a moist adiabat as shown in Fig. 4A. The atmospheric state (i.e. mean thermal structure) at the end of this first phase (i.e. when the first droplet of water reaches the ground) depends on the amount of CO_2 and H_2O in the atmosphere, but does not depend on the initial post-impact temperature assumed. This means that, for the impact event described here (1 bar CO_2 atmosphere + 2 bar of water vaporized), the initial temperature (here, 500 K) does not have any major effect on the nature of the environmental effects (on the atmosphere and the surface, but not the subsurface) of the impact during the following phases (phases II, III

[2] We explore in Sections 3 and 4 how the initial water and CO_2 content affect the impact-induced climate change.

[3] Although the choice of the post-impact temperature seems arbitrary here, we show in Section 3.1 that the impact-induced climate state becomes independent of initial post-impact temperature from the moment the first droplet of liquid water hits the ground. The temperature is then controlled by the condensation temperature of the water vapour (determined by the Clausius-Clapeyron equation) and not the initial post-impact temperature.

and IV described below). The duration of this first phase is roughly controlled by (i) the net Top Of Atmosphere (TOA) radiative budget and (ii) the amount of extra thermal energy of the atmosphere (i.e. the difference of thermal energy between the initial post-impact thermal profile - here a 500 K isotherm thermal profile - and a moist adiabatic thermal profile.). The duration of this phase is usually short because the initially hot atmosphere quickly cools by emitting thermal radiation to space. For our reference simulation, it takes $\sim$0.5 martian year[4] for the first droplet of water to reach the surface, which sets the end of this first phase (see Fig. 1A). This phase is not interesting from the point of view of surface erosion because no water is present at the surface.

Phase II: hot atmosphere, intense precipitation. This second phase starts when the atmosphere becomes almost entirely saturated in water vapour, and water can start to rain on the surface and accumulate. This phase ends when most water vapour has condensed on the surface. This is the most interesting phase because it coincides with the main bulk of precipitation (rainfall). During this phase, our 3-D Global Climate simulations indicate that (1) a thick, reflective and quasi-uniform cloud cover is present and (2) the net radiative budget at the Top Of the Atmosphere (TOA) is roughly constant, because both the outgoing longwave radiation (OLR) and the planetary albedo are constant (see Fig. 1B). For our reference simulation, the net TOA radiative budget is -180 W/m^2 (indicating the planetary atmosphere must cool to reach equilibrium). As a result, the water vapour atmospheric content gets progressively depleted (see Fig. 1C). The duration of this second phase is roughly controlled by (i) the net TOA radiative budget and (ii) the total amount of latent heat that can be extracted from the condensation of the entire water vapour atmospheric column. For our reference simulation, the duration of the phase is $\sim$12 martian years. This duration can be empirically approximated by $q_{\mathrm{col,H_2O}}(m)/4.5$, where $q_{\mathrm{col,H_2O}}$ is the initial global mean integrated column of water vapour in GEL (m). Approximately 2.6 m of water condenses on the surface per Earth year, which is very similar to the result obtained by Segura et al. (2002) with a 1-D cloud-free numerical climate model. This rainfall rate is constant during phase II (because the net TOA disequilibrium is constant) indicating that the rainfall rate does not depend on the initial water inventory (as long as water is a radiatively dominant atmospheric species). Note that the surface evaporation of water is very limited during this phase. In our reference simulation, approximately 8% of the precipitation gets re-evaporated from the surface (see Fig. 1D). We investigate this phase in more details in the next subsections.

Phase III: conversion of surface liquid water into ice. When the third phase starts, most water vapour has already condensed on the surface. Surface water rapidly freezes and the planet gets cold (see Fig. 1A), even colder than before the impact event because the planet is now covered by a thick, reflective ice cover (this ice cover is actually expected to be thicker in the topographic lows, i.e. basins and the northern lowlands where liquid water would flow during phase II). Based on the results of Turbet et al. (2017a), water - that should accumulate in the topographic depressions of the planet - would freeze (down to the bottom) in 10^3–10^5 years maximum (depending on the total water content).

Phase IV: migration of water ice to the cold traps. In the fourth phase, water progressively migrates to the cold traps of the planet. For our reference simulation (high CO_2 atmospheric pressure, high obliquity), water should migrate to the southern highlands (Bouley et al., 2016; Turbet et al., 2017a; Wordsworth et al., 2013). We do not explicitly simulate this phase here. However, based on the results of Turbet et al. (2017a), water should migrate to the cold traps of the planet within 10^4–10^6 years (depending on the total water content).

In total, it takes $\sim$15 martian years for the surface temperature to drop below the freezing temperature of water (273 K). Note that subsurface temperatures could remain above 273 K for much longer periods of time, as reported in Segura et al. (2002). At the end of our simulations (after $\sim$18 martian years), the mean (regolith) subsurface temperatures at 5 and 50 m are respectively 320 and 470 K.

Steakley et al. (2019) recently independently presented a similar chronology of events (also in four distinct phases) derived from 3-D Global Climate Model simulations of smaller impactors.

Below we investigate in much more details the second phase, because this is the phase in which most of the precipitation (rainfall) occurs.

3.2. Clouds and radiative budget

The second phase starts when the first droplet of (liquid) water reaches the surface of Mars. At this stage, the atmosphere is almost entirely saturated in water vapour. The outgoing longwave radiation (OLR) is roughly constant through time (see Fig. 1B) and across the planet. The OLR is dominated by the thermal infrared emission of the moist, upper atmosphere (see Fig. 3D). This result is similar in nature with the asymptotic behaviour of the OLR predicted by 1-D radiative convective models assuming a thermal profile following the water vapour saturation curve (Kasting et al., 1993; Kopparapu et al., 2013; Nakajima et al., 1992). This is the typical state reached by planets entering in runaway greenhouse. For a Mars-size planet, Kopparapu et al. (2014) estimates that the asymptotic OLR (for a pure water vapour atmosphere) is 250 W/m^2, i.e. 20 W/m^2 higher than our result. This small difference is likely due to (i) a different CO_2 atmospheric content (discussed in the next section; see also Goldblatt and Watson, 2012, Ramirez et al., 2014b and Marcq et al., 2017), (ii) different treatments of water vapour absorption (Kopparapu et al., 2013), (iii) the radiative effect of clouds in the infrared.

Thermal radiation cooling occurs mainly in the upper atmospheric layers (see Fig. 3D). This triggers moist convection and thus water vapour condensation, forming clouds in the upper atmosphere (see Fig. 3A–C). Because this radiative cooling occurs everywhere (at each latitude and longitude of the planet), clouds form everywhere on the planet (see Figs. 2 and 3A). This result is qualitatively in agreement with Segura et al. (2008). Moreover, simple energy conservation consideration (supported by our 3-D Global Climate simulations) show that approximately 1 kg/m^2 of cloud particles are produced every 3 h. The production rate of cloud particles is so high that cloud particles accumulate, growing to large sizes up to several hundreds of microns for icy particles in the upper cloud layer (see Fig. 3C). The accumulation of cloud particles is limited by (i) coagulation of cloud liquid droplets into raindrops (following the numerical scheme of Boucher et al., 1995) and (ii) sedimentation of large ice particles (parameterized following a Stokes law (Rossow, 1978)). As a result, our 3-D Global Climate simulations show that a thick, uniform cloud cover is produced in the upper layers of the planet (see Fig. 3A–C).

This thick, uniform cloud cover (mostly located in the upper atmosphere, as illustrated in Fig. 3A and B) reflects incoming solar radiation efficiently. In average, the planetary albedo reaches $\sim$0.55 (see Fig. 1B). Moreover, a large fraction of the incoming solar radiation is absorbed in the upper atmospheric layers, mostly by water vapour and clouds. As a result, the strong deficit of absorbed solar radiation versus outgoing longwave radiation (see Fig. 1B) cools down the planet very rapidly. During most of this phase, the radiative disequilibrium at the top of the atmosphere is ~ -180 W/m^2. As a result, the atmosphere and the planet progressively cool down (see Figs. 1A and 2).

As the planet cools down, the globally averaged cloud water content and visible opacity slowly decrease (see Fig. 1E and F). While water is progressively raining out from the atmosphere, the atmosphere is

[4] One martian year lasts approximately 687 Earth days, i.e. 1.88 Earth years.

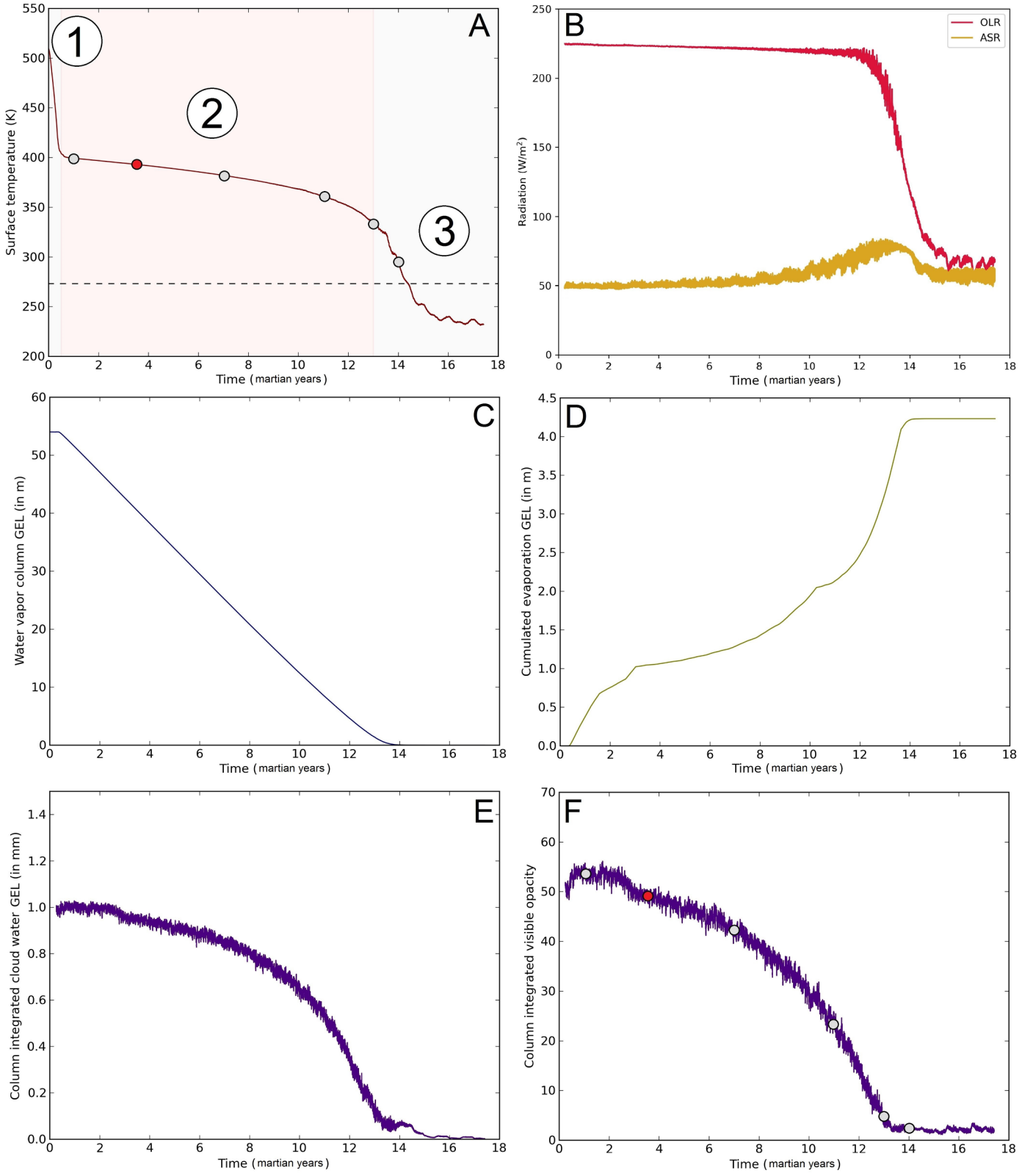

Fig. 1. Globally averaged temporal evolution of the (A) surface temperature (in K), (B) top of atmosphere radiative fluxes (in W/m^2), (C) integrated column of water vapour (in m GEL), (D) cumulative surface evaporation of water (in m GEL), (E) column integrated cloud water content (in mm GEL) and (F) column integrated cloud visible opacity. All these quantities were computed for the reference simulation described extensively in Section 3 of this paper. The grey/pink zones (and numbers 1, 2, 3) in panel A indicate the three first post-impact phases described in Section 3.1. (For interpretation of the references to color in this figure legend, the reader is referred to the web version of this article.)

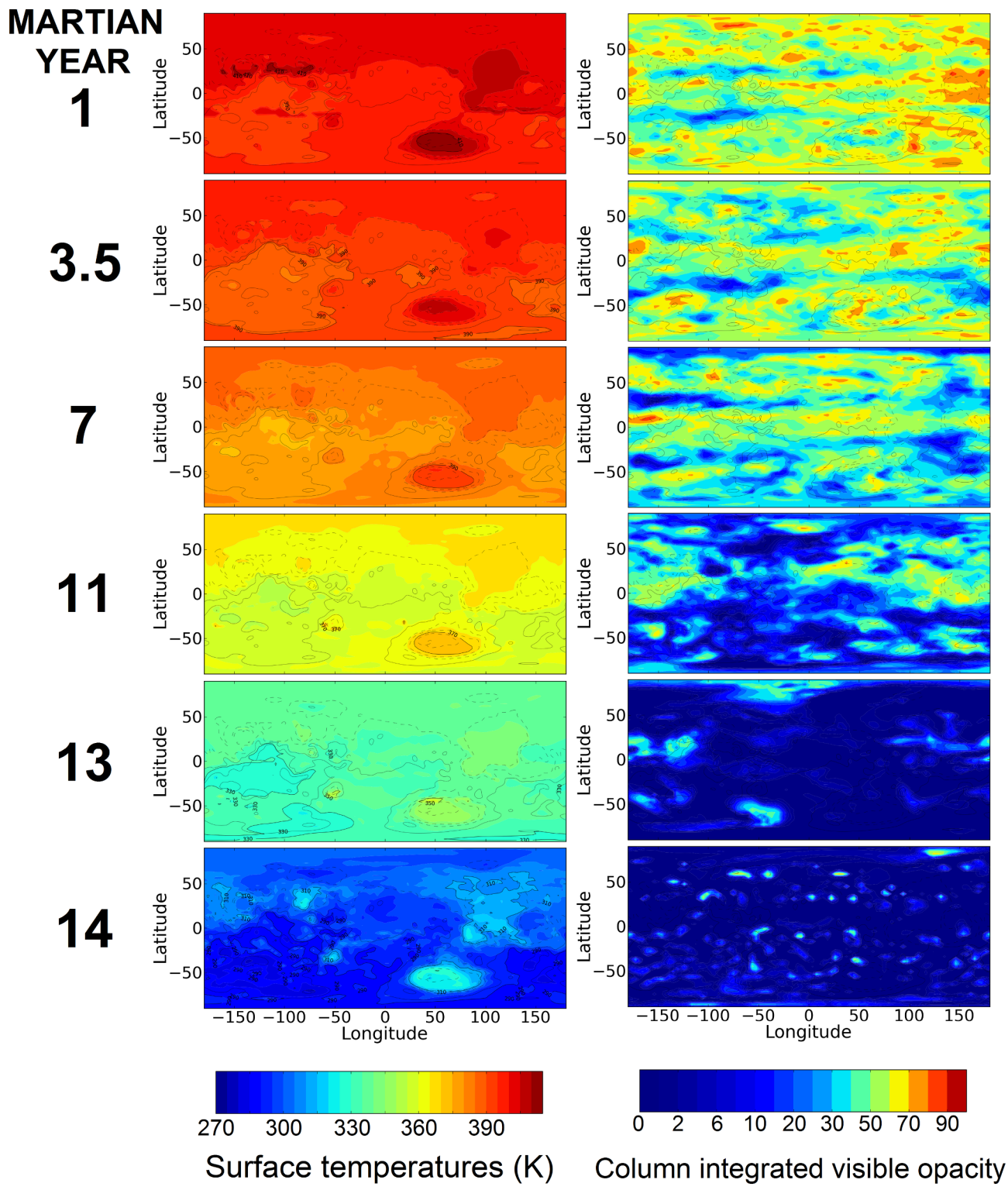

Fig. 2. Snapshots of post-impact surface temperature (in K) and visible opacity maps at six distinct timings (1, 3.5, 7, 11, 13 and 14 martian years). These six timings are also highlighted in Fig. 1A and F with dots.

progressively drying out. The upper atmosphere become slowly drier through time, producing more and more unsaturated regions. Progressively, we enter in a regime of radiative fins as predicted by Pierrehumbert (1995) and simulated with a 3-D Global Climate Model in Leconte et al. (2013) in the context of the runaway greenhouse, where the emission can locally exceed the maximum emission for a saturated atmosphere. This can be observed in Fig. 2 (right panel) where the clouds become more and more patchy through time. Regions where clouds are absent coincide (i) with sub-saturated regions and (ii) with regions where the thermal emission to space exceeds the maximum emission ($\sim 230\ W/m^2$, here) calculated for a quasi-saturated atmosphere.

While the planet cools down, not only the globally averaged surface temperature decreases, but also the variability of the surface

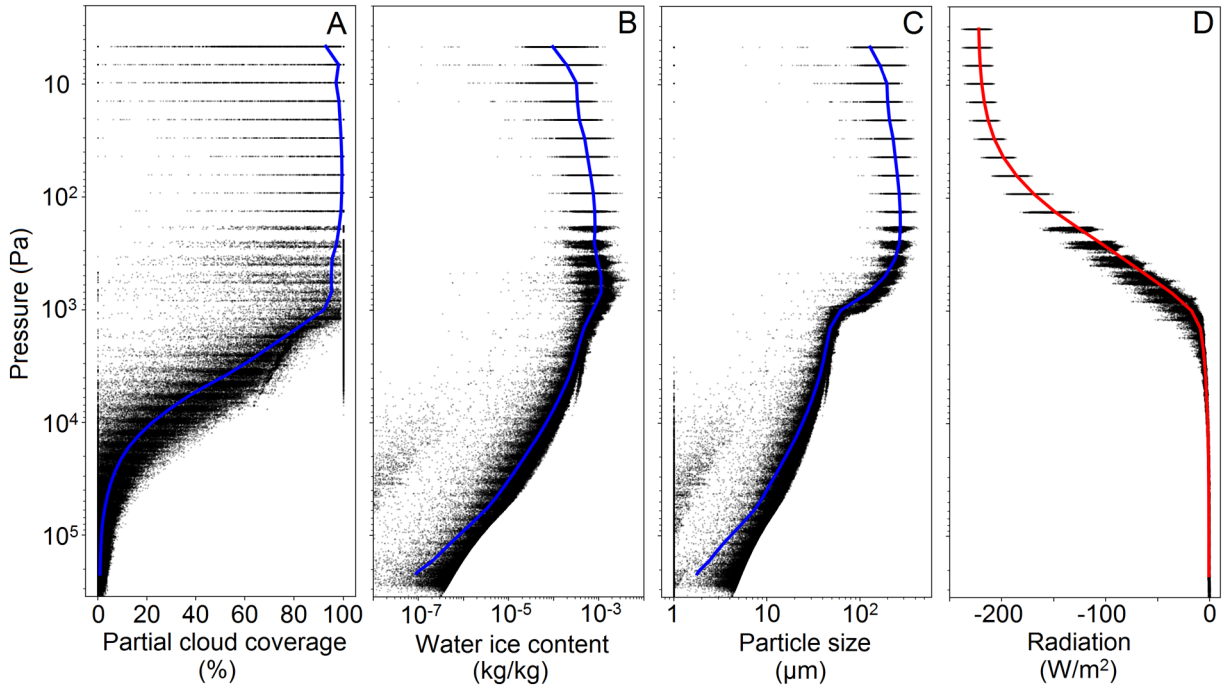

Fig. 3. Vertical profiles of (A) the partial cloud coverage (in %), (B) the water ice content (in kg/kg), (C) the effective radius of cloud particles (in μm) and (D) the net thermal infrared flux passing through each of the atmospheric layer (negative means upward). These profiles are snapshots calculated 3.5 martian years after the impact event. This timing is highlighted in Fig. 1 with a red dot. The colored thick lines vertical profiles are globally averaged snapshots. Small black dots are snapshots of all possible values reached by GCM air cells. In total, there are 276,480 (i.e. the number of GCM air cells) black dots in each subfigure. Note that comb-like structures appear because fixed pressure levels were used in the upper atmosphere (see Section 2.1).

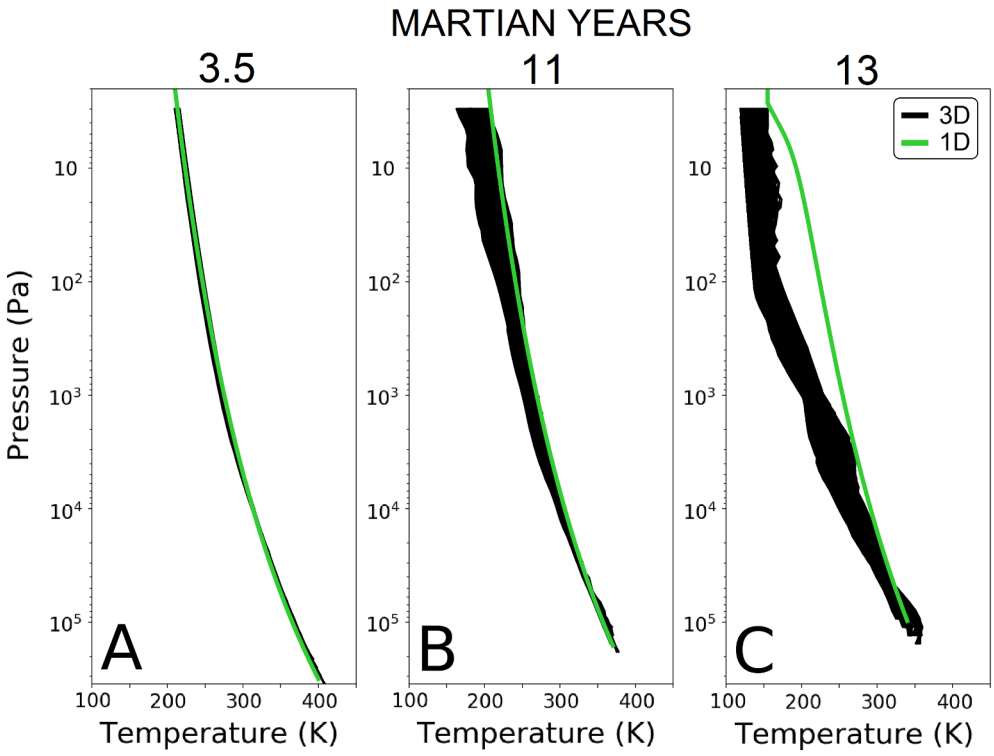

Fig. 4. Snapshots of the vertical thermal profiles after 3.5 (left panel), 11 (middle panel) and 13 martian years (right panel). The black region indicates all the {pressure,temperature} reached in the 3-D Global Climate simulation. The green solid line indicates the thermal profile calculated in our 1-D inverse climate model (see description in Section 2.2) for the same surface temperature and CO_2 partial pressure as assumed in the GCM reference simulation. (For interpretation of the references to color in this figure legend, the reader is referred to the web version of this article.)

temperature and more generally of the atmospheric temperature progressively increases (see Fig. 4A–C). During most of the second phase, the 1D thermal (and water vapour, respectively) profiles calculated at each location of the planet in the GCM follow remarkably well the thermal (and water vapour, respectively) profile predicted by 1D climate calculations (see Fig. 4A) assuming a fully saturated profile. But as the planet cools down, subsaturated regions appear and discrepancies with the 1-D calculations start to emerge (see Fig. 4B and C). The fact that the thermal and water vapour profiles match very well 1-D calculations during most of the second phase is important, because it indicates that we can use a 1-D model (computationally much more efficient than 3-D simulations) to explore the nature of the post-impact

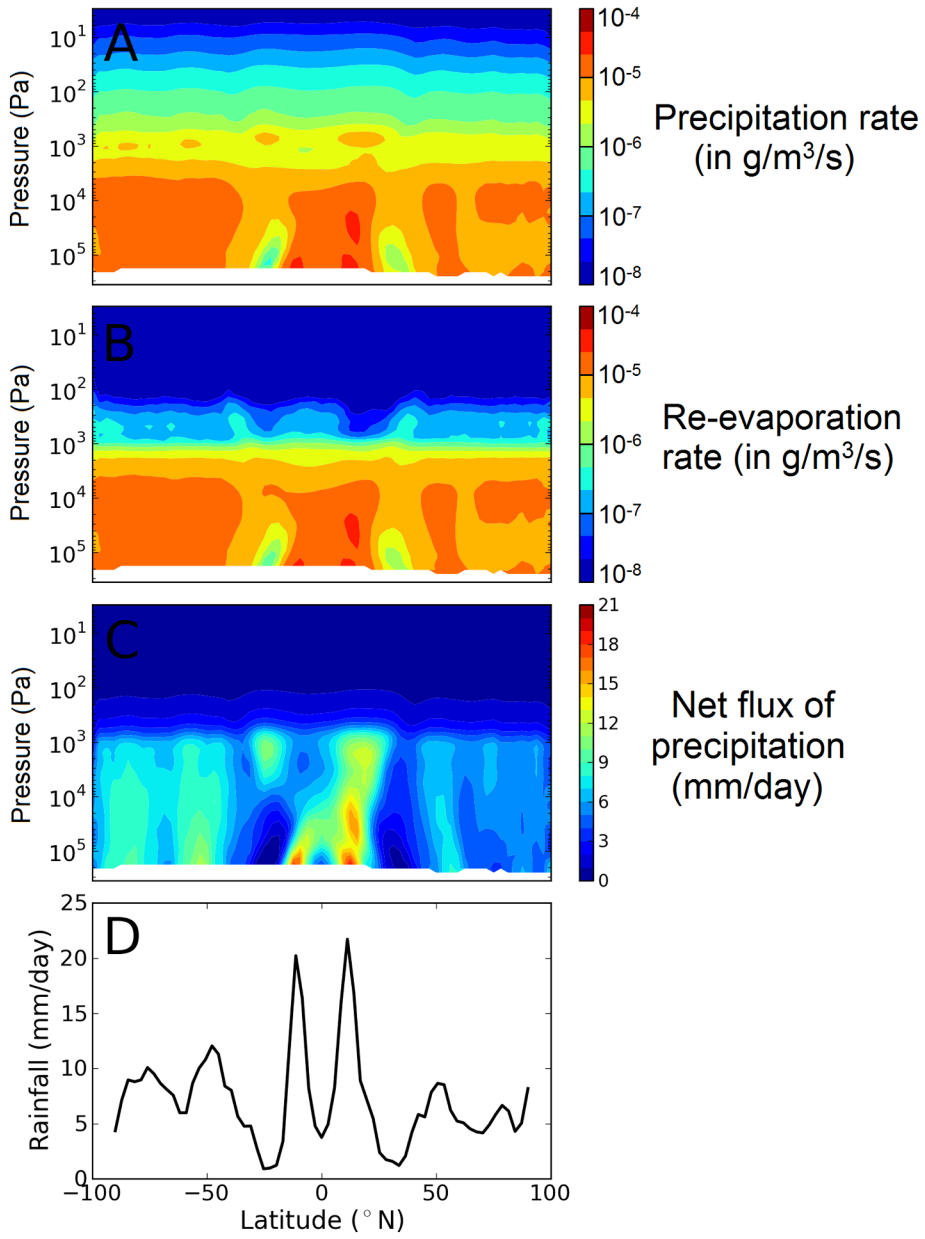

Fig. 5. Snapshot of the zonal means of (A) the cloud particle rate of precipitation (in g/m^3/s), (B) the rate of re-evaporation of precipitation (in g/m^3/s), (C) the downward flux of precipitation (accounting for re-evaporation) in kg/m^2/day (or mm/day) and (D) the surface accumulation of precipitation (in mm/day). This is a snapshot 3.5 martian years after the reference impact event.

main phase of precipitation, depending on many different parameters (e.g. CO_2 and H_2O total atmospheric contents). This exploration is the topic of Section 4.

3.3. Localization of precipitation

Precipitation is produced uniformly in the upper cloud layer. Yet, most of the precipitation of the main, upper cloud layer is re-evaporated while falling through some sub-saturated lower layers (following the numerical scheme of Gregory, 1995). This is illustrated in Fig. 5 that presents a snapshot of the zonal mean budget of precipitation/re-evaporation. In fact, 3-D GCM simulations indicate that almost none of the precipitation produced in the upper cloud layer actually reaches the surface (see Fig. 5). Instead, this is the condensation produced by the large scale air movements in the lower atmosphere that is the primary source of precipitation reaching the ground of the planet.

The equatorial regions receive (in our 3-D simulations) in average a few tens of W/m^2 of solar radiation in excess compared to the poles. This is likely enough to trigger large scale movements in the lower atmosphere, in particular to transport energy from the equator to higher latitudes, following a Hadley cell-like structure. Near the equator, ascending air produces condensation and thus precipitation (see Fig. 5D). Near 30°S/30°N latitudes, this is the descending branch of the Hadley cell. These regions of air subsidence are noticeably sub-saturated, and (almost) no precipitation reaches the ground (see Fig. 5D).

Fig. 6 illustrates the fact that the precipitation (rainfall) patterns are mostly produced in response to the large scale circulation in the lower atmosphere. We note a peak of precipitation near the equator (ascending branch of Hadley cell) and a lack of precipitation near 30°S/30°N (descending branch of Hadley cell). As a result, the precipitation pattern recorded in the 3-D simulation is intriguingly anti-correlated with the position of the valley networks (located around 30°S) mapped in the pre-True Polar Wander topography (Bouley et al., 2016). Future

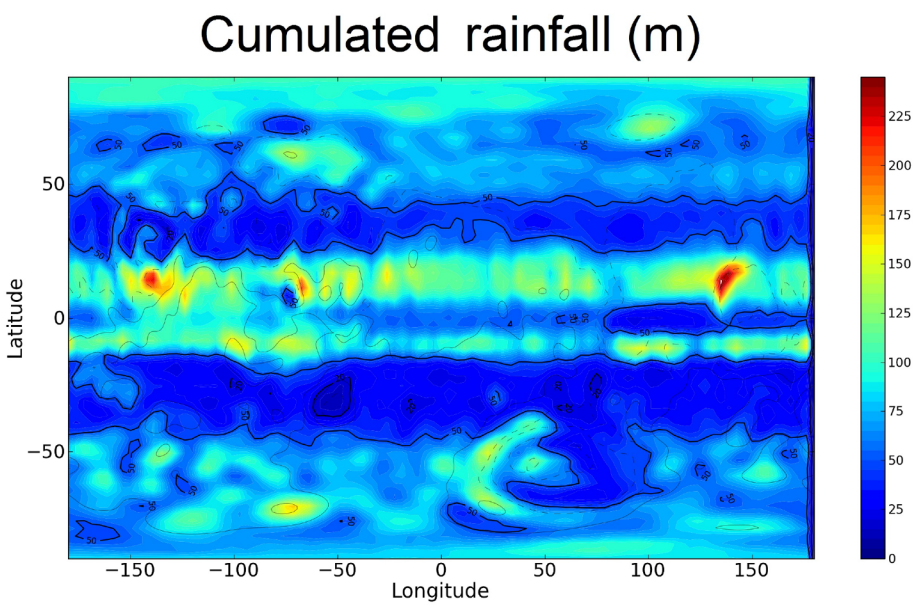

Fig. 6. Cumulative rainfall map (in m) 15 martian years after the bolide impact event. Ascending branches of the Hadley cells lie near the equator, while descending branches are located around ± 30° latitude. The absence of rain at the equator is due to the presence of equatorially trapped modes producing westerly winds.

work could better explore how the latitudinal distribution of incoming solar radiation (e.g. due to different obliquity) or other source of forcing can impact the lower atmospheric circulation and thus the precipitation patterns. Significant precipitation is also recorded at higher latitudes, likely produced by large scale atmospheric circulation. In addition, we also note some localized sources of precipitation (e.g. east of Hellas crater) or absences of precipitation (e.g. bottom of Argyre crater) likely due to coupling between lower atmospheric circulation and topography (e.g. through adiabatic cooling on the crater slopes, or intense re-evaporation of precipitation at the bottom of deep craters). Our 3-D numerical simulations suggest though that the topographic effect of large basins (e.g. Hellas, Argyre, Isidis) has a minimal contribution to the large-scale-circulation-induced precipitation patterns discussed here.

In average, ~58 m of precipitation (54 m from the initial water vapour reservoir, 4 m from evaporation of precipitation that reached the ground) is recorded throughout the 3-D simulations. Note that, although there are some latitudinal differences in the surface distribution of precipitation, cumulative precipitation is high everywhere on the planet (at least 20 m of cumulative precipitation). Precipitation is deluge-like with an average of 2.6 m of precipitation per Earth year. Such heavy rains are incompatible with the formation of martian valley networks (Barnhart et al., 2009). However, they could produce overland flow, which could be responsible for Noachian crater degradation (Palumbo and Head, 2018).

Moreover, because most of the precipitation that reaches the ground does not get re-evaporated, the impact-induced hydrological cycle is a 'one-shot' cycle (i.e. there is a low amount of hydrological cycling of water). The low amount of surface evaporation is due to the fact that the lower atmosphere is close to saturation during the second phase (hot atmosphere, intense precipitation) of the impact event. We acknowledge that we did not take into account the possibility that water could be transported from wetter to drier latitudes possibly through river flow, which may increase surface evaporation in the driest regions of the planet (e.g. near ± 30° latitude). However, we believe this should not significantly increase the total surface re-evaporation of precipitation, because the lower atmosphere is close to saturation even in the driest regions of the planet. At first order, the total amount of rainfall produced in response to a very large impact event can be approximated by the total amount of water vapour initially vaporized and/or sublimed in the atmosphere, i.e. by the total (near-surface,surface) Noachian water content. Thus, the amount of rainfall produced by basin-scale impact events is orders of magnitude lower than that required for valley network formation (Luo et al., 2017; Rosenberg et al., 2019), even when accounting for all observed Noachian-aged basins.

4. Exploration of the diversity of post-impact atmospheres with a 1-D inverse climate model

3-D simulations are great to explore in details the post-impact atmospheric evolution due to atmospheric circulation, formation and evolution of clouds, etc. but are not suited (due to their high computational cost) to explore the sensitivity of the results to a wide range of parameters. We demonstrated in the previous section that the thermal profiles of the atmosphere in the GCM are well reproduced by 1D radiative-convective calculations during the main post-impact phase of precipitation (see Fig. 4A and B). Here we use a 1-D radiative-convective inverse climate model presented in Section 2.2 to explore the sensitivity of the results obtained with our 3-D Global Climate Model.

The initial post-impact CO_2 and H_2O atmospheric reservoirs are highly uncertain because they depend on the pre-impact CO_2 atmospheric pressure and (near-surface,surface) water reservoirs, as well as the amount and nature of volatiles delivered and excavated by the impactor[5]. The water cloud properties (size of particles, thickness of clouds) are also highly uncertain because they depend on many exotic physical processes that are not properly modeled in the GCM. Thus, we want to explore how (i) the total CO_2 and H_2O initial inventories and (ii) the microphysics of clouds can affect the TOA (Top of Atmosphere) radiative budget and thus the duration of the impact-induced climate change.

4.1. Results from cloud-free numerical climate simulations

We first explore cloud-free numerical climate simulations to investigate the role of the initial, post-impact CO_2 and H_2O atmospheric inventories. Here we vary two parameters: the initial surface

[5] It has been recently proposed (Haberle et al., 2017) that fast thermochemical reactions that take place in the very hot post-impact martian atmosphere could produce H_2 and CH_4 that could generate afterwards an efficient CIA-induced greenhouse effect (Turbet et al., 2019; Wordsworth et al., 2017). This effect is not modeled here, but deserves further investigations.

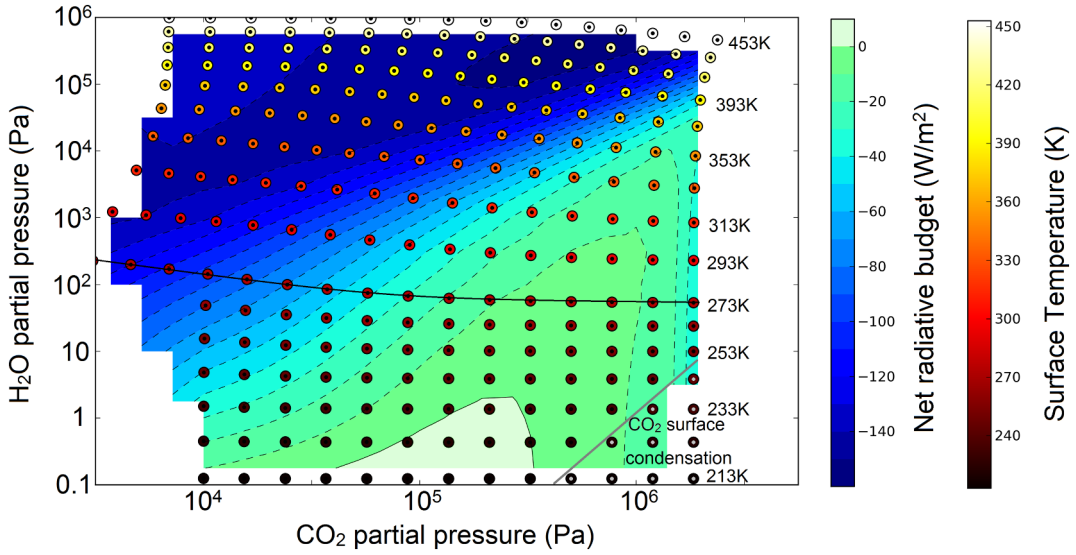

Fig. 7. Contour plot of the net radiative budget at the TOA (Top Of Atmosphere) of the post-impact early Mars atmosphere, as a function of CO_2 and H_2O partial pressures in the atmosphere. The contour plot was calculated by interpolating the data points of the scatter plot. The color of the data points corresponds to the surface temperature of the simulation. The planet is at equilibrium if the radiative budget is equal to 0, which is never the case for any of the post-impact simulations. For a given CO_2 atmospheric content, the increase in H_2O content leads to a decrease in the net TOA radiative budget despite the greenhouse effect of water vapour. This is due to the fact that the surface temperature also increases, which increases the OLR and decreases the net radiative budget at the TOA. This dependency stops when the OLR reaches its asymptotic value. (For interpretation of the references to color in this figure legend, the reader is referred to the web version of this article.)

temperature (from 213 to 453 K) and the initial atmospheric pressure (from 3 mbar to 30 bar). Cold temperatures (< 240 K) are typical of global mean pre-impact surface temperatures calculated for CO_2-dominated atmospheres (Forget et al., 2013; Wordsworth et al., 2013). Warm temperatures (> 240 K) are typical of post-impact surface temperatures expected during the main phase of precipitation (corresponding to the second phase depicted in Section 3.1). As a comparison, we recall that the maximum post-impact temperature recorded in our 3-D reference simulation (discussed in the previous section) during the precipitation phase is ~400 K. Because we assume that water vapour is saturated everywhere in the atmosphere (except in the isothermal [155 K] stratosphere, whenever a stratosphere exists), the total water vapour content and thus the atmospheric CO_2 content can be calculated a posteriori. In our 1-D simulations, the total water vapour partial pressure ranges approximately between 0.1 Pa and 10 bar, and the CO_2 partial pressure between 3 mbar and 25 bar, in order to cover a wide range of possible post-impact atmospheric states.

From these simulations, we calculated the radiative disequilibrium at the top of the atmosphere (TOA) for various combinations of CO_2 and H_2O atmospheric contents, summarized in Fig. 7. Our results are unequivocal. Whatever the amount of water vapour, CO_2 in the atmosphere, and whatever the initial post-impact temperature assumed, the atmosphere is always out of equilibrium, and there is no long-term greenhouse-induced self-maintained warm climate induced by the impact.

The only balanced solutions are found for very low surface temperatures (below 230 K), for CO_2 partial pressures on the order of a few bar, recovering the cold surface temperatures predicted by 1-D simulations of early Mars assuming CO_2/H_2O atmospheres (Ramirez et al., 2014a; Turbet and Tran, 2017; Wordsworth et al., 2010). These solutions result from a subtle balance between the greenhouse effect of CO_2, CO_2 atmospheric condensation and CO_2 Rayleigh scattering.

In the upper part of the diagram, the outgoing longwave radiation (OLR) has an asymptotic behaviour whatever the CO_2 atmospheric pressure, whenever water vapour is a dominant species. At 1 bar of CO_2 and 2 bar of H_2O, we match the reference case described with the 3-D Global Climate Model in the previous section. The OLR and absorbed solar radiation (ASR) are 235 and 85 W/m^2, respectively, which gives a TOA radiative disequilibrium of −150 W/m^2. The radiative disequilibrium is 30 W/m^2 less than calculated in the 3-D simulation (see Fig. 1B). Although we recover a very similar OLR, the ASR is much higher (+30 W/m^2) in the 1-D simulation. The difference is likely due to the fact that the 3-D simulation accounts for the albedo of the thick cloud cover forming in the upper atmosphere, whereas clouds are not taken into account in the 1-D simulations presented in this subsection.

We confirm the result obtained in the previous section (with the 3-D GCM) that whenever water vapour becomes a dominant species, the OLR reaches asymptotic values (see Fig. 7) that are very similar to those calculated by 1-D climate models for moist atmospheres in or near the runaway greenhouse (Kopparapu et al., 2013, 2014). The fact that the OLR reaches – in the water-rich limit – an asymptotic value much larger than the solar flux possibly absorbed by early Mars is a strong argument against the Segura et al. (2012) hypothesis, i.e. that stable runaway greenhouse states are stable on early Mars. Although two stable solutions (one cold, one warm) are indeed predicted by calculations assuming purely radiative H_2O-dominated atmospheres, the warm solution should be physically implausible (Goldblatt and Watson, 2012; Ingersoll, 1969; Nakajima et al., 1992) when convection and condensation processes are considered. First, this warm solution requires water vapour supersaturation levels that are extremely high (see Goldblatt and Watson, 2012, Figure 2), so high that they lie well above the maximum supersaturation limits (even imposed by homogeneous nucleation) of water vapour (Pruppacher and Klett, 1996). Secondly, these purely radiative calculations neglect convective processes that control the thermal structure of the atmosphere. Whenever (i) convection processes are included and (ii) water vapour is limited by saturation, the bistability disappears and we recover the Nakajima limit (Goldblatt and Watson, 2012; Nakajima et al., 1992), i.e. the asymptotic behaviour of the OLR at the runaway greenhouse.

Whatever the initial reservoir of CO_2 and the amount of H_2O produced in response to the impact event, the duration of the warm period (i.e. for surface temperatures above the freezing point of water) is short. Fig. 7 provides estimates of the radiative disequilibrium at the TOA for many different combinations of CO_2 and H_2O reservoirs. These TOA radiative disequilibriums can be used to estimate the duration of the post-impact warm periods. For instance, for a 1 bar CO_2 atmosphere (similar to the 3-D reference simulation), the duration of the warm period (around 10–20 martian years) is very similar to that calculated

with a 3D Global Climate Model. More generally, our calculations are in rather good agreement with the 1-D cloud-free climate calculations of Segura et al. (2002) and Segura et al. (2008).

The duration of the impact-induced warm period increases with increasing CO_2 atmospheric content (see Fig. 7) because as CO_2 atmospheric levels increase, the temperature - at a given atmospheric pressure - decreases. This results from the fact that the atmospheric temperature - at saturation - is governed by the partial pressure of water vapour (and not the total pressure). As a result, adding CO_2 cools the upper atmosphere, which drastically reduces the OLR. Fig. 7 indicates that, for atmospheres made of 10+ bar of CO_2, the net TOA radiative budget could be reduced by a factor of ten and the duration of the impact-induced warm period could thus increase by a factor of ten, compared to the reference simulation presented in Section 3. However, such high CO_2 atmospheric contents are unlikely (Forget et al., 2013; Kite, 2009).

4.2. Results from cloudy numerical climate simulations

We now include in our 1-D simulations the radiative effect of a cloud cover (as described in Section 2.2). We use these simulations to explore how cloud microphysics (that depends in our 3-D Global Climate Model on the assumed number of cloud condensation nucleis [CCNs], and on the efficiency of the coagulation and sedimentation processes) could affect the results presented in the previous section.

4.2.1. The radiative effect of water ice clouds: comparison with Ramirez and Kasting (2017)

We first compare the results of our 1-D inverse cloudy climate model in 'temperate' (surface temperature fixed to 273 K) conditions with the results of Ramirez and Kasting (2017). Ramirez and Kasting (2017) used a very similar model to explore if cirrus clouds could have warmed the surface of early Mars above the melting point of water. Fig. 8 shows a comparison of the results of our model with theirs using similar assumptions. Whenever data points are available, the agreement between the two models is really good. We note a slight difference for the bond albedo of low altitude clouds (affecting subsequently the calculation of the effective flux S_{eff}; see Fig. 8B and D) that is likely due to slight differences in the (visible) radiative properties of water ice particles.

Ramirez and Kasting (2017) intentionally limited the maximum altitude of clouds explored in their simulations to the top of the (H_2O) moist convective region. Above, they claimed that production of water ice clouds should be unfeasible. This is why they did not provide any data point for pressures smaller than 0.15 bar. As a result, Ramirez and Kasting (2017) did not capture the radiative effects of water ice clouds above the hygropause, although injections of water ice particles could be produced for example in response to extreme events such as bolide impact events as discussed in Urata and Toon (2013). Interestingly, this corresponds exactly to the altitude where the radiative effect of clouds is maximum (see Fig. 8C). This is not surprising because this is where the cloud temperature is minimal. For this reason, the linear interpolations proposed in Figures 2, 5, 8, 9 and 11 of Ramirez and Kasting (2017) should be interpreted with great care by the readers.

Assuming that water ice clouds can exist above the hygropause, our model predicts that only a few tens of % of global cloud coverage should be sufficient to raise the surface of Mars above 273 K. This is illustrated in Fig. 9A that shows the minimum cloud coverage needed to reach a surface temperature of 273 K in the simulation (assuming a 1 km-thick cloud cover) depending on the surface pressure, cloud particle sizes and relative ice cloud water content (compared to the IWC [Ice Water Content]) defined in Section 2.2. In theory, water ice cloud particles above the hygropause could thus warm early Mars above the melting point of water easily, even for relatively low (and thus reasonable) cloud coverage.

However, we do not want to give the reader the impression that this provides a satisfactory scenario to warm early Mars. For clouds to be stable at such high altitudes, a strong mechanism must be at play to replenish the upper atmosphere in cloud particles that are expected to sedimentate rapidly (Ramirez and Kasting, 2017). The strong greenhouse warming of water ice clouds reported by Segura et al. (2008) and

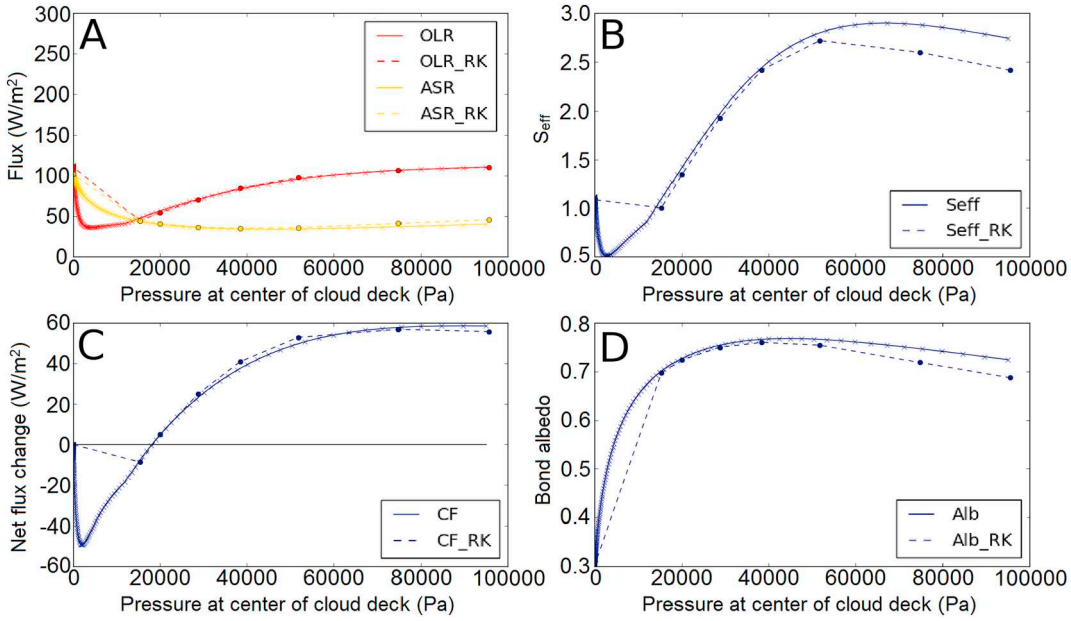

Fig. 8. Effect of a single cloud layer on the radiative budget of early Mars, as a function of the pressure at the center of the cloud deck. (A) Outgoing Longwave Radiation (OLR) and Absorbed Solar Radiation (ASR); (B) effective solar flux S_{eff}; (C) net flux change between cloudy and non-cloudy cases; (D) bond albedo. The dashed lines correspond to the results of Ramirez and Kasting (2017) (presented in their Figure 2 and Table 1b). The solid lines correspond to the results obtained with our 1-D inverse climate model. We assumed here a 1 bar CO_2 dominated atmosphere (fully saturated in H_2O, except in the stratosphere [if present]). The cloud layer is assumed to be composed only of 10 μm cloud particles. The surface temperature is assumed to be that of the freezing point of water, i.e. 273 K. The solar flux is assumed to be that of present-day Mars. Note that the effective solar flux corresponds to the value of the solar flux (with respect to the Solar constant on Mars) required for the planet to be at the TOA radiative balance.

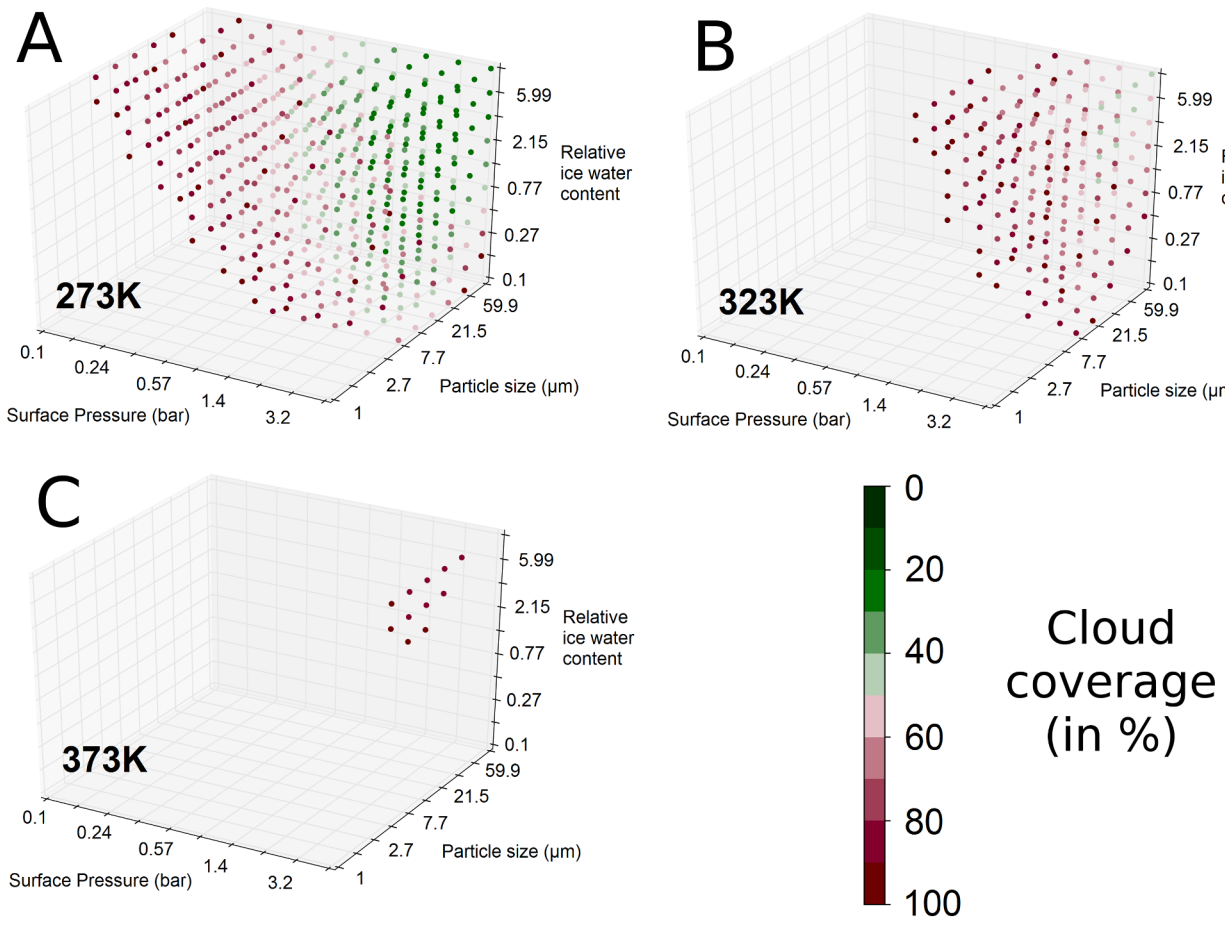

Fig. 9. 3-D scatter plots of the minimal cloud coverage required to warm early Mars above the indicated post-impact surface temperatures (273, 323 and 373 K), for various CO_2 atmospheric pressure, relative ice water content (i.e. cloud thickness) and cloud particle size. Fractional cloud cover is modeled by averaging the radiative fluxes from cloudy and cloud-free 1-D simulations. No dot was plotted for sets of parameters unable to warm the planet above the indicated surface temperature even with a 100% cloud coverage. We provide in Fig. 12 (Appendix) 2-D cross-sections of these 3-D scatter plots.

Urata and Toon (2013) is likely due to the fact that they neglected the sedimentation of ice particles. This hypothesis is supported by back of the envelope calculations of sedimentation rates of icy particles (Ramirez and Kasting, 2017), and confirmed by our 3-D Global Climate model simulations. As soon as the initial impact-induced water vapour reservoir is depleted, the production rate of cloud particles drops and upper atmosphere water ice clouds rapidly disappear because of gravitational sedimentation. Therefore, the lack of sedimentation is the most reasonable hypothesis to explain the difference between Segura et al. (2008), Urata and Toon (2013) and our results. Until a plausible, long lasting source or mechanism of replenishment of upper atmospheric water ice clouds is evidenced, the strong water ice cloud greenhouse warming reported by Segura et al. (2008) and Urata and Toon (2013) is unlikely.

4.2.2. Post-impact 1-D cloudy simulations

We showed in Section 3.2 (using our 3-D climate simulations) that a thick, complete impact-induced cloud cover can be sustained in the upper atmosphere of early Mars for most of the duration of the main phase of precipitation following a large impact event. During this phase, surface temperatures are significantly higher than the value of 273 K explored above. Here we investigate how the cloud properties (size of particles, cloud thickness, etc.) can change the radiative effect of the impact-induced cloud cover and thus the net TOA radiative budget, during the post-impact main phase of precipitation.

Because we showed in the previous sections that (1) the thermal profiles calculated with our 1-D inverse climate model match very well those derived from 3-D Global Climate Model simulations during the main phase of precipitation, and that (2) the inclusion of a cloud layer in our 1-D model gives satisfactory results with regards to the existing literature (Ramirez and Kasting, 2017) for a surface temperature of 273 K, we can now safely apply our 1-D cloudy numerical climate simulations to higher post-impact surface temperatures ($T > 273$ K). We use these simulations to investigate the radiative effect of the thick, complete cloud cover predicted by 3-D simulations.

Our findings are summarized in Fig. 9, that presents the minimal cloud coverage required to warm the surface of early Mars above the indicated surface temperatures (323 and 373 K). For the two surface temperatures considered, there is at least one combination of parameters (cloud altitude, cloud particles, cloud content and surface pressure) that can stably keep the surface temperature of early Mars above the indicated post-impact temperatures (323 and 373 K). However, although the constraints on (i) the possible total cloud coverage and (ii) the maximum altitude of the cloud layer are relaxed during the main post-impact phase of precipitation (as demonstrated with 3-D simulations in Section 3.2), the range of parameters that provide a positive radiative balance gets narrower as the surface temperature increases. In fact, the solutions that work - at high post-impact surface temperatures - are limited to very thick multi-bar CO_2-dominated atmospheres[6] endowed with a very thick cloud cover located very high in

[6] This behaviour can be understood by looking back at Fig. 7 that shows that for post-impact cloud-free atmospheres, and for a fix water content/surface temperature, increasing the initial CO_2 atmospheric content decreases the TOA

the atmosphere, for cloud particles around 10 µm in size. This very restrictive set of conditions - although it could theoretically lead to a self-sustained impact-induced warm atmosphere - seems extremely difficult to attain.

5. Exploration of the long-term effects of a very large impactor on the interior of Mars with a 2-D mantle dynamics numerical model

Large impacts affect a planet like Mars on a broad range of timescales. Although its atmosphere reacts over a relatively short period, large collisions can modify the interior evolution of the planet over millions to billions of years. Since the interior and exterior of Mars interact, surface conditions are also affected by the consequences of impacts on all timescales. In order to complete the picture of environmental consequences of large impacts on Mars, we included simulations of mantle dynamics effects of those events using the StagYY numerical code described in Section 2.4.

We considered projectiles in the range of 200–500 km diameter (i.e., producing crater diameter of 1000–2500 km; Toon et al., 2010); with our reference case set at 300 km (crater diameter of 1500 km). Projectiles significantly smaller than the reference case ($D_{impactor} < 200$ km, i.e. $D_{crater} < 1000$ km) only have a marginal effect on mantle dynamics. Global changes in convection patterns are seen mainly if $D_{impactor} > 500$ km (i.e. $D_{crater} > 2500$ km), but such impacts are outside the range of observed events for the present work (see Gillmann et al., 2016). Impactor velocities range from 5.1 to 20 km/s, with a reference case set to 9 km/s.

For high velocity cases, the impact-induced thermal anomaly can reach temperatures up to 5000 K. Fig. 10 illustrates that the anomaly decreases after the peak on a timescale of $\sim 10^7$ years. The maximum temperature of the anomaly is 3500 K and 2700 K after 1 and 10 million years, respectively. After the emplacement of the buoyant temperature anomaly, a stage of thermal relaxation occurs, where the hot zone flattens under the surface of the planet and widens, recovering qualitatively the results of Gillmann et al. (2016) on Venus and of Ruedas and Breuer (2017, 2018, 2019) on Mars.

Partial melting of the mantle occurs in the interior, where the thermal anomaly is maximum, i.e. near the impact location. The liquid melt-pond produced by the impact heating is in contact with the atmosphere and convects vigorously, as a consequence, it loses heat very efficiently and freezes quickly compared to the typical timescale of mantle convection (Reese and Solomatov, 2006; Solomatov, 2015). This produces the formation of a basaltic crust whose thickness is maximum at the location of the impact. Consequently, the crust is locally thickened, which reduces the efficiency of the heat transfer (Lenardic et al., 2004) near the impact location. This thick basaltic crust acts as an insulating layer in a comparable way to the effect of continents on Earth (Coltice et al., 2009).

Fig. 11 shows the evolution of the heat flux across the surface following the large, reference bolide impact. At the impact location, the thermal anomaly is very strong but the surface internal heat flux is low[7] (much lower than before the impact) and can drop below 10 mW/m^2 for several tens of millions years (see Fig. 11) because of the insulation produced by the basaltic crust. At the edge of the impact location, the thermal anomaly is still high, but low enough to limit the melting and thus the production of insulating basaltic crust[8]. As a result, the internal heat flux can reach several hundreds of mW/m^2 or $\sim$10 times the ambient flux (see Fig. 11) at the edge of the impact location for several millions of years. Far from the impact location, the thermal anomaly is too low to significantly affect the internal heat flux.

In summary, although the surface internal heat flux can be very strong at the location of the impact for 10^2–10^3 years (Segura et al., 2002), on the longer term this flux drastically drops below 10 mW/m^2 for tens of millions of years. Besides, the internal heat flux significantly increases up to several hundreds mW/m^2 (i.e. up to $\sim$10 times the ambient flux) on the edges of the impact crater for millions of years. Although such internal heat fluxes are orders of magnitude too low to keep the martian surface above the melting point of water, they could have had an impact on the subsurface hydrothermal system and on the basal melting of ice deposits (that could have accumulated on the impact crater edges through atmospheric processes, described in Phase IV; see Section 3.1). We leave this study for future work.

6. Conclusions and discussions

We explored in this manuscript the environmental effects of the largest impact events recorded on Mars using a hierarchy of numerical models, ranging from a 1-D radiative-convective inverse model to a full 3-D Global Climate Model and a 2-D Mantle Dynamics model.

Our results indicate that the duration of the impact-induced warm period (in the atmosphere and at the surface) is usually very short, because the radiative budget at the Top Of the Atmosphere (TOA) is in strong deficit. Whatever the initial CO_2 atmospheric content and whatever the size of the impactor, we show that the impact-induced stable runaway greenhouse state predicted by Segura et al. (2012) is physically inconsistent.

For an early martian atmosphere made of 1 bar of CO_2, a large impact would produce $\sim$2.6 m of surface precipitation per Earth year, until the reservoir of water vapour gets completely depleted. This is quantitatively similar to the results of Segura et al. (2002), obtained using a 1-D cloud free climate model. Surface evaporation of precipitation is weak (i.e. low amount of hydrological cycling of water) and as a result, the total amount of precipitation produced in response to the impact event can thus be well approximated by the total amount of water vapour initially vaporized and/or sublimed in the atmosphere (from the impactor, the impacted terrain and from the sublimation of permanent ice reservoirs heated by the hot ejecta layer).

3-D simulations show that an optically thick, upper atmospheric cloud cover forms uniformly on the planet. Our 3-D simulations - taking into account simplified cloud microphysics - indicate that this cloud cover contributes to a net cooling of the surface of Mars, compared to cloud-free calculations. Although strong precipitation is generated in this cloud cover, most of it is re-evaporated in the atmosphere while falling. Instead, surface precipitation patterns are governed by lower atmospheric large scale circulation. In our 3-D simulations, precipitation (rainfall) is maximum near the equator, at the ascending branch of the Hadley cell, and are minimum near the tropics, at the descending branch. Although the cumulative amount of precipitation is rather high everywhere on the planet (at least 20 m of cumulative precipitation), we find that the main region of valley networks formation on Mars (located around -30°S in the pre-TPW topography, see Figure 1 in Bouley et al., 2016) coincides with a minimum of cumulative precipitation in our 3-D simulations (see Fig. 6). We confirm the results of Segura et al. (2008) and Urata and Toon (2013) that water ice clouds

(*footnote continued*)
radiative disequilibrium. For example, for a surface temperature of 373K, and a CO_2 initial surface pressure of 10 bar, the net TOA radiative disequilibrium is ~ -40 W/m^2.

[7] The internal heat flux could be very strong in the near subsurface for 10^2–10^3 years (Segura et al., 2002), due to the residual of the near-surface impact-induced thermal anomaly as well as the hot ejecta deposited all over the planet. Another effect to consider is the potential impact melt sea that will collect on the floor of the basin, and that can take a longer time to cool to equilibrium (Cassanelli and Head, 2016; Vaughan and Head, 2014; Vaughan et al., 2013) These effects are not captured by the StagYY code which explores the effects of the impact on much longer timescales.

[8] The impact-induced ejecta layer deposited over the martian surface could also insulate part of the interior. This effect is not accounted in our 2-D Mantle Dynamics simulation.

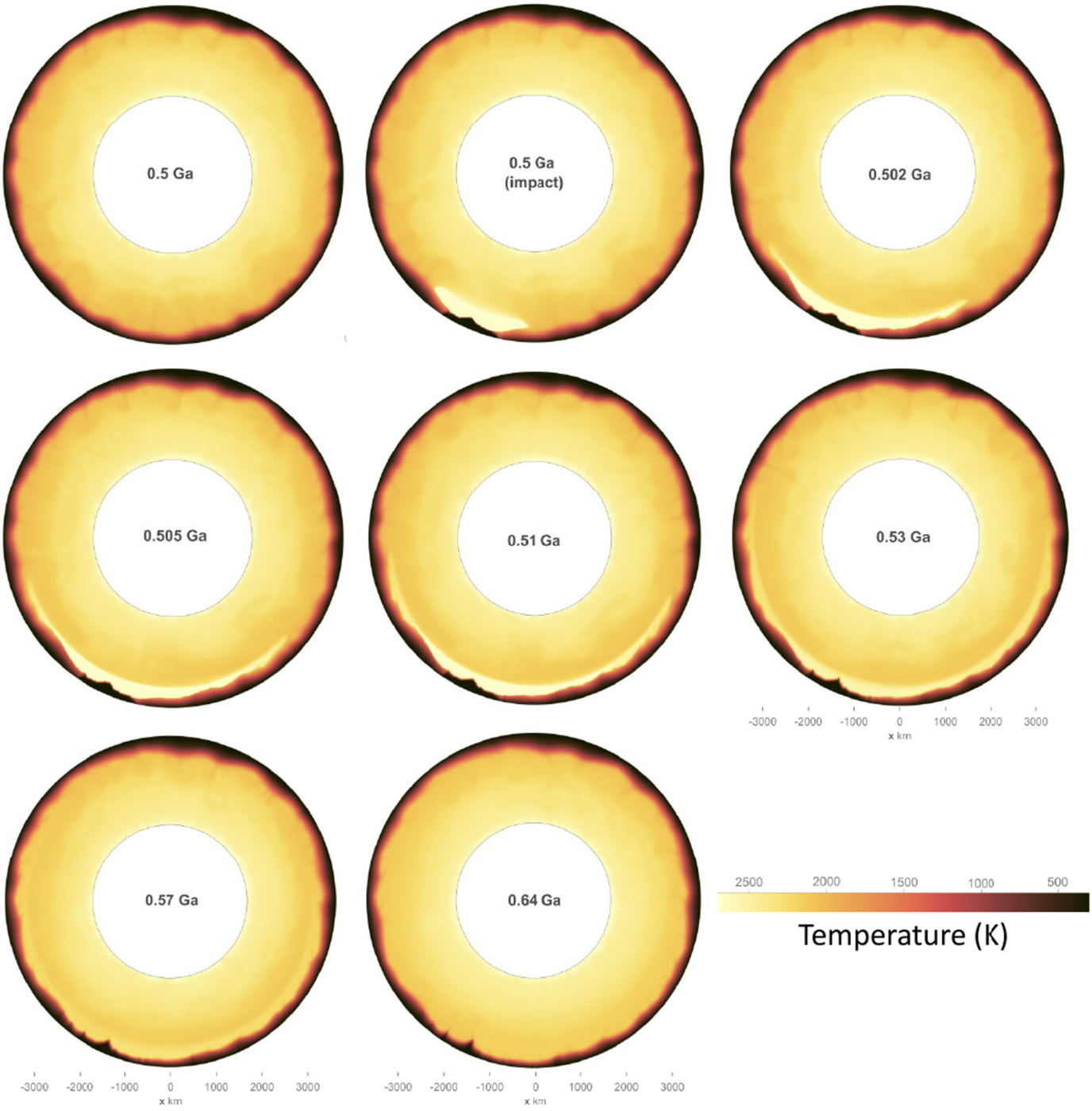

Fig. 10. Evolution of the martian mantle temperature following a 300 km diameter impactor (roughly corresponding to a crater diameter of 1500 km, using Toon et al., 2010 scaling relationship) hitting the surface of Mars (reference case). The velocity of the impactor is set to set to 9 km/s for the reference case.

could in theory significantly extend the duration of the post-impact warm period, and for significantly lower cloud coverage than predicted in Ramirez and Kasting (2017). However, as soon as the main bulk of the water vapour reservoir has condensed on the surface, the production rate of upper atmospheric cloud particles drops, and high altitude water ice clouds dissipate because of gravitational sedimentation. This prevents the water ice cloud greenhouse warming mechanism from working. We also find that the duration of the impact-induced warm period increases with increasing CO_2 atmospheric content. For instance, the duration can be increased by a factor 10 for a 10 bar CO_2 atmosphere (with respect to a 1 bar CO_2 atmosphere). However, such high CO_2 contents are unlikely (Forget et al., 2013; Kite, 2009).

In summary, the environmental effects of the largest impact events recorded on Mars are characterized by (i) a short impact-induced warm period, (ii) a low amount of hydrological cycling of water (because the evaporation of precipitation that reached the ground is extremely limited), (iii) precipitation patterns that are uncorrelated with the observed regions of valley networks formation, and (iv) deluge-style precipitation.

On the long-term, we find that large bolide impacts can produce a strong thermal anomaly in the mantle of Mars that can survive and propagate for tens of millions of years. This thermal anomaly could raise the near-surface internal heat flux up to several hundreds of mW/m^2 (i.e. up to ~10 times the ambient flux) for several millions years at

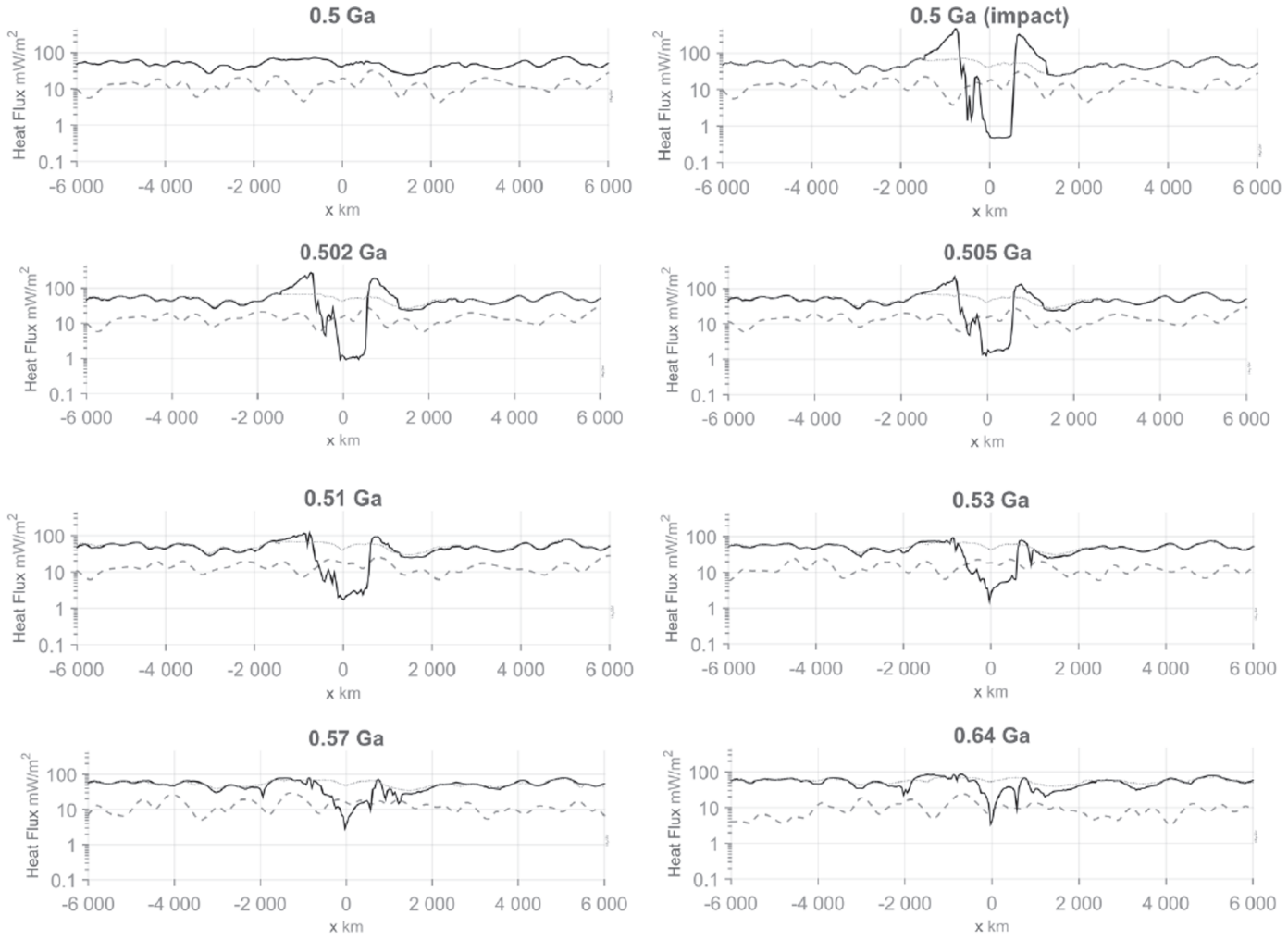

Fig. 11. Evolution of the near-surface internal heat flux (in mW m^{-2}) following a 300 km diameter impactor (i.e. a crater diameter of 1500 km, using Toon et al., 2010 scaling relationship) hitting the surface of Mars (black line), as a function of the distance to the impact crater. The grey, dotted line indicates the near-surface internal heat flux for the reference simulation without impact. The grey, dashed line indicates the internal heat flux at the Core Mantle boundary (CMB). Note that the internal heat flux at the CMB is weakly affected by the impact.

the edges of the impact crater. However, such internal heat flux is largely insufficient to keep the martian surface above the melting point of water.

In addition to the poor temporal correlation between the formation of the largest basins and valley networks (Fassett and Head, 2011), these arguments indicate that the largest impact events are unlikely to be the direct cause of formation of the Late Noachian valley networks. Our numerical results support instead the prediction of Palumbo and Head (2018) that such deluge-style rainfall could have caused crater degradation of large craters, erased small craters, and formed smooth plains, potentially erasing much of the previously visible morphological surface history. Such hot rainfalls may have also led to the formation of aqueous alteration products on Noachian-aged terrains (Palumbo and Head, 2018), which is consistent with the timing of clays that were expected to have formed in situ (e.g. Carter et al., 2015).

Acknowledgments

This work was granted access to the HPC resources of the Institute for Computing and Data Sciences (ISCD) at Sorbonne Universite. This work benefited from the IPSL ciclad-ng facility. We are grateful for the computing resources on OCCIGEN (CINES, French National HPC). C. Gillmann was supported by BELSPO's Planet TOPERS IAP programme and FNRS's ET-HOME EOS programme. We thank P. Tackley for the use of his mantle dynamics code StagYY and for his advice. The geodynamic diagnostics and scientific visualisation software StagLab (Crameri, 2017, 2018) is used in this study. M.T. thanks Fuxing Wang, Frederique Cheruy, Jim Kasting and the LMD Planeto team for useful discussions related to this work. This project has received funding from the European Union's Horizon 2020 - Research and Innovation Framework Programme under the Marie Sklodowska-Curie Grant Agreement No. 832738/ESCAPE. M.T. would like to thank the Gruber Foundation for its generous support to this research.

Appendix A. Additional figure

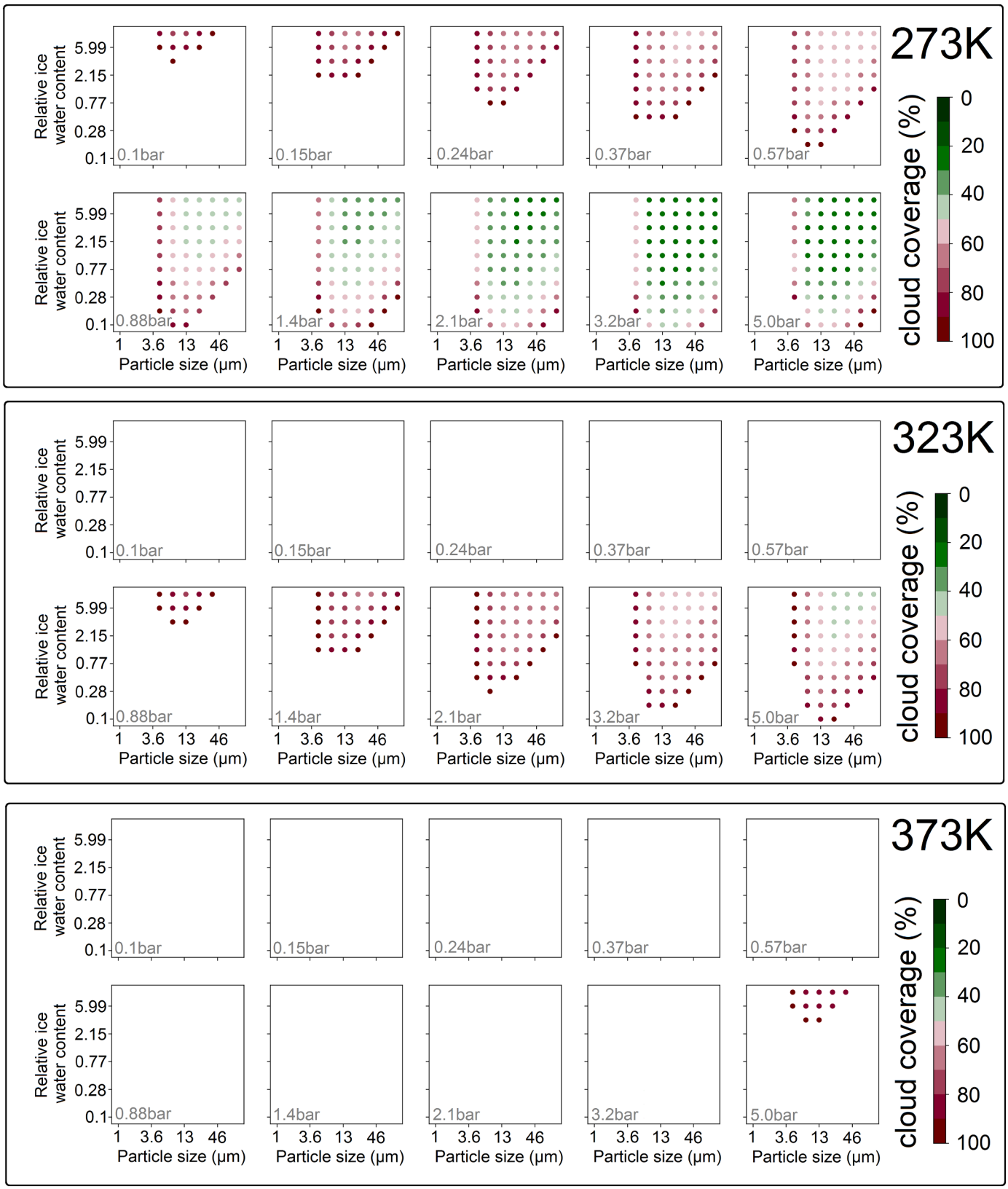

Fig. 12. 2-D scatter plots of the minimal cloud coverage required to warm early Mars above the indicated post-impact surface temperatures (273, 323 and 373 K), for various CO_2 atmospheric pressure, relative ice water content (i.e. cloud thickness) and cloud particle size. These 2-D scatter plots are cross-sections of 3-D scatter plots presented in Fig. 9, for 10 distinct CO_2 surface pressures.

References

Armann, M., Tackley, P.J., 2012. Simulating the thermochemical magmatic and tectonic evolution of Venus's mantle and lithosphere: two-dimensional models. J. Geophys. Res. Planets 117 (E12003).

Baranov, Y.I., Lafferty, W.J., Fraser, G.T., 2004. Infrared spectrum of the continuum and dimer absorption in the vicinity of the O_2 vibrational fundamental in O_2/CO_2 mixtures. J. Mol. Spectrosc. 228, 432–440.

Barnhart, C.J., Howard, A.D., Moore, J.M., 2009. Long-term precipitation and late-stage valley network formation: landform simulations of Parana Basin, Mars. J. Geophys. Res. Planets 114 (E01003).

Bibring, J.-P., Langevin, Y., Mustard, J. F., Poulet, F., Arvidson, R., Gendrin, A., Gondet, B., Mangold, N., Pinet, P., Forget, F., 2006. Global Mineralogical and Aqueous Mars History Derived From OMEGA/Mars Express Data, 312, 400–404.

Boucher, O., Le Treut, H., Baker, M.B., 1995. Precipitation and radiation modeling in a general circulation model: introduction of cloud microphysical processes. J. Geophys. Res. 100, 16.

Bouley, S., Baratoux, D., Matsuyama, I., Forget, F., Séjourné, A., Turbet, M., Costard, F., 2016. Late Tharsis formation and implications for early Mars. Nature 531, 344–347.

Brown, L.R., Humphrey, C.M., Gamache, R.R., 2007. CO_2-broadened water in the pure rotation and ν_2 fundamental regions. J. Mol. Spectrosc. 246, 1–21.

Cabrol, N.A., Grin, E.A., 1999. Distribution, classification, and ages of martian impact crater lakes. Icarus 142, 160–172.

Carr, M.H., 1995. The martian drainage system and the origin of valley networks and fretted channels. J. Geophys. Res. 100, 7479–7507.

Carr, M.H., Head, J.W., 2015. Martian surface/near-surface water inventory: sources, sinks, and changes with time. Geophys. Res. Lett. 42, 726–732.

Carter, J., Loizeau, D., Mangold, N., Poulet, F., Bibring, J.-P., 2015. Widespread surface weathering on early Mars: a case for a warmer and wetter climate. Icarus 248, 373–382.

Carter, J., Poulet, F., Bibring, J.-P., Mangold, N., Murchie, S., 2013. Hydrous minerals on Mars as seen by the CRISM and OMEGA imaging spectrometers: updated global view. J. Geophys. Res. Planets 118, 831–858.

Cassanelli, J.P., Head, J.W., 2016. Did the Orientale impact melt sheet undergo large-scale igneous differentiation by crystal settling? Geophys. Res. Lett. 43, 11.

Charnay, B., 2014, Tropospheric Dynamics and Climatic Evolution of Titan and the Early Earth. Theses, Universite Pierre et Marie Curie - Paris VI.

Coltice, N., Bertrand, H., Rey, P., Jourdan, F., Phillips, B.R., Ricard, Y., 2009. Global warming of the mantle beneath continents back to the Archaean. Gondw. Res. 15, 254–266.

Craddock, R.A., Howard, A.D., 2002. The case for rainfall on a warm, wet early Mars. J. Geophys. Res. Planets 107, 1–21.

Crameri, F., 2017, Staglab 3.0, The development of StagLab is supported by the Research Council of Norway through its Centers of Excellence funding scheme, Project Number 223272.

Crameri, F., 2018. Geodynamic diagnostics, scientific visualisation and Staglab 3.0. Geosci. Model Dev. 11 (6), 2541–2562.

Delahaye, T., Landsheere, X., Pangui, E., Huet, F., Hartmann, J.-M., Tran, H., 2016. Broadening of CO_2 lines in the 4.3 μm region by H_2O. J. Mol. Spectrosc. 326, 17–20.

Ding, F., Pierrehumbert, R.T., 2016. Convection in condensible-rich atmospheres. Astrophys. J. 822 (24).

Ehlmann, B.L., Mustard, J.F., Murchie, S.L., Bibring, J.-P., Meunier, A., Fraeman, A.A., Langevin, Y., 2011. Subsurface water and clay mineral formation during the early history of Mars. Nature 479, 53–60.

Eymet, V., Coustet, C., Piaud, B., 2016. kspectrum: an open-source code for high-resolution molecular absorption spectra production. J. Phys. Conf. Ser. 676 (1) 012005.

Fassett, C.I., Head, J.W., 2008. The timing of martian valley network activity: constraints from buffered crater counting. Icarus 195, 61–89.

Fassett, C.I., Head, J.W., 2011. Sequence and timing of conditions on early Mars. Icarus 211, 1204–1214.

Forget, F., Wordsworth, R., Millour, E., Madeleine, J.-B., Kerber, L., Leconte, J., Marcq, E., Haberle, R.M., 2013. 3D modelling of the early martian climate under a denser CO_2 atmosphere: temperatures and CO_2 ice clouds. Icarus 222, 81–99.

Fu, Q., Liou, K.N., 1992. On the correlated k-distribution method for radiative transfer in nonhomogeneous atmospheres. J. Atmos. Sci. 49, 2139–2156.

Galperin, B., Kantha, L.H., Hassid, S., Rosati, A., 1988. A quasi-equilibrium turbulent energy model for geophysical flows. J. Atmos. Sci. 45, 55–62.

Gamache, R.R., Farese, M., Renaud, C.L., 2016. A spectral line list for water isotopologues in the 1100–4100 cm^{-1} region for application to CO_2-rich planetary atmospheres. J. Mol. Spectrosc. 326, 144–150.

Gillmann, C., Golabek, G.J., Tackley, P.J., 2016. Effect of a single large impact on the coupled atmosphere-interior evolution of Venus. Icarus 268, 295–312.

Gillmann, C., Tackley, P., 2014. Atmosphere/mantle coupling and feedbacks on Venus. J. Geophys. Res. Planets 119, 1189–1217.

Goldblatt, C., Watson, A.J., 2012. The runaway greenhouse: implications for future climate change, geoengineering and planetary atmospheres. Trans. R. Soc., A 370, 4197–4216.

Gregory, D., 1995. A consistent treatment of the evaporation of rain and snow for use in large-scale models. Mon. Weather Rev. 123, 2716.

Grotzinger, J.P., Gupta, S., Malin, M.C., Rubin, D.M., Schieber, J., Siebach, K., Sumner, D.Y., Stack, K.M., Vasavada, A.R., Arvidson, R.E., Calef, F., Edgar, L., Fischer, W.F., Grant, J.A., Griffes, J., Kah, L.C., Lamb, M.P., Lewis, K.W., Mangold, N., Minitti, M.E., Palucis, M., Rice, M., Williams, R.M.E., Yingst, R.A., Blake, D., Blaney, D., Conrad, P., Crisp, J., Dietrich, W.E., 2015. Deposition, exhumation, and paleoclimate of an ancient lake deposit, Gale crater, Mars. Science 350.

Gruszka, M., Borysow, A., 1997. Roto-translational collision-induced absorption of CO_2 for the atmosphere of Venus at frequencies from 0 to 250 cm^{-1}, at temperatures from 200 to 800 K. Icarus 129, 172–177.

Haberle, R.M., Catling, D.C., Carr, M.H., Zahnle, K.J., 2017. The Early Mars Climate System Cambridge Planetary Science. Cambridge University Press, pp. 526–568.

Haberle, R.M., Zahnle, K., Barlow, N., 2017. Impact eelivery of reduced greenhouse gases on early Mars. In: Fourth International Conference on Early Mars: Geologic, Hydrologic, and Climatic Evolution and the Implications for Life. LPI Contributions. vol. 2014. pp. 3022.

Hynek, B.M., Beach, M., Hoke, M.R.T., 2010. Updated global map of martian valley networks and implications for climate and hydrologic processes. J. Geophys. Res. Planets 115, E09008.

Ingersoll, A.P., 1969. The runaway greenhouse: a history of water on Venus. J. Atmos. Sci. 26, 1191–1198.

Karato, S.-I., Jung, H., 2003. Effects of pressure on high-temperature dislocation creep in olivine. Philos. Mag. 83, 401–414.

Kasting, J.F., Pollack, J.B., Ackerman, T.P., 1984. Response of earth's atmosphere to increases in solar flux and implications for loss of water from Venus. Icarus 57, 335–355.

Kasting, J.F., Whitmire, D.P., Reynolds, R.T., 1993. Habitable zones around main sequence stars. Icarus 101, 108–128.

Keller, T., Tackley, P.J., 2009. Towards self-consistent modeling of the martian dichotomy: the influence of one-ridge convection on crustal thickness distribution. Icarus 202, 429–443.

Kite, E.S., 2019. Geologic constraints on early Mars climate. Space Sci. Rev. 215, 10.

Kite, E.S., Gao, P., Goldblatt, C., Mischna, M.A., Mayer, D.P., Yung, Y.L., 2017. Methane bursts as a trigger for intermittent lake-forming climates on post-Noachian Mars. Nat. Geosci. 10, 737–740.

Kopparapu, R.K., Ramirez, R., Kasting, J.F., Eymet, V., Robinson, T.D., Mahadevan, S., Terrien, R.C., Domagal-Goldman, S., Meadows, V., Deshpande, R., 2013. Habitable zones around main-sequence stars: new estimates. Astron. J. 765, 131.

Kopparapu, R.K., Ramirez, R.M., SchottelKotte, J., Kasting, J.F., Domagal-Goldman, S., Eymet, V., 2014. Habitable zones around main-sequence stars: dependence on planetary mass. The Astrophysical Journal Letters 787, L29.

Laskar, J., Correia, A.C.M., Gastineau, M., Joutel, F., Levrard, B., Robutel, P., 2004. Long term evolution and chaotic diffusion of the insolation quantities of Mars. Icarus 170, 343–364.

Leconte, J., Forget, F., Charnay, B., Wordsworth, R., Pottier, A., 2013. Increased insolation threshold for runaway greenhouse processes on Earth-like planets. Nature 504, 268–280.

Lenardic, A., Nimmo, F., Moresi, L., 2004. Growth of the hemispheric dichotomy and the cessation of plate tectonics on Mars. J. Geophys. Res. Planets 109, E02003.

Luo, W., Cang, X., Howard, A.D., 2017. New martian valley network volume estimate consistent with ancient ocean and warm and wet climate. Nat. Commun. 8, 15766.

Ma, Q., Tipping, R.H., 1992. A far wing line shape theory and its application to the foreign-broadened water continuum absorption. III. J. Chem. Phys. 97, 818–828.

Madeleine, J.-B., 2011 Dust and Clouds on Mars: Remote Sensing, Modeling of Climate Feedbacks and Paleoclimate Applications. Theses, Université Pierre et Marie Curie - Paris VI. Manuscrit soumis aux rapporteurs le 15 Décembre 2010 et accepté sans modification majeures. La version finale ne comporte que des changements mineurs.

Malin, M.C., Edgett, K.S., 2003. Evidence for persistent flow and aqueous sedimentation on early Mars. Science 302, 1931–1934.

Manabe, S., 1969. Climate and the ocean circulation. Mon. Weather Rev. 97, 739.

Manabe, S., Wetherald, R., 1967. Thermal equilibrium of the atmosphere with a given distribution of relative humidity. jas 24, 241–259.

Mangold, N., Adeli, S., Conway, S., Ansan, V., Langlais, B., 2012. A chronology of early Mars climatic evolution from impact crater degradation. J. Geophys. Res. Planets 117, E04003.

Mangold, N., Ansan, V., 2006. Detailed study of an hydrological system of valleys, a delta and lakes in the Southwest Thaumasia region, Mars. Icarus 180, 75–87.

Marcq, E., Salvador, A., Massol, H., Davaille, A., 2017. Thermal radiation of magma ocean planets using a 1-D radiative-convective model of H_2O-CO_2 atmospheres. J. Geophys. Res. Planets 122, 1539–1553.

Mellor, G.L., Yamada, T., 1982. Development of a turbulence closure model for geophysical fluid problems. Rev. Geophys. Space Phys. 20, 851–875.

Mlawer, E.J., Payne, V.H., Moncet, J.-L., Delamere, J.S., Alvarado, M.J., Tobin, D.C., 2012. Development and recent evaluation of the MT_CKD model of continuum absorption. Philos. Trans. R. Soc. London, Ser. A 370, 2520–2556.

Monteux, J., Coltice, N., Dubuffet, F., Ricard, Y., 2007. Thermo-mechanical adjustment after impacts during planetary growth. Geophys. Res. Lett. 34, L24201.

Moore, J.M., Howard, A.D., Dietrich, W.E., Schenk, P.M., 2003. Martian layered fluvial deposits: implications for Noachian climate scenarios. Geophys. Res. Lett. 30, 2292.

Mustard, J.F., Murchie, S.L., Pelkey, S.M., Ehlmann, B.L., Milliken, R.E., Grant, J.A., Bibring, J.-P., Poulet, F., Bishop, J., Dobrea, E.N., Roach, L., Seelos, F., Arvidson, R.E., Wiseman, S., Green, R., Hash, C., Humm, D., Malaret, E., McGovern, J.A., Seelos, K., Clancy, T., Clark, R., Marais, D.D., Izenberg, N., Knudson, A., Langevin, Y., Martin, T., McGuire, P., Morris, R., Robinson, M., Roush, T., Smith, M., Swayze, G., Taylor, H., Titus, T., Wolf, M., 2008. Hydrated silicate minerals on Mars observed by the Mars Reconnaissance Orbiter CRISM instrument. Nature 454, 305–309.

Nakagawa, T., Tackley, P.J., 2004. Effects of thermo-chemical mantle convection on the thermal evolution of the Earth's core. Earth Planet. Sci. Lett. 220, 107–119.

Nakajima, S., Hayashi, Y.-Y., Abe, Y., 1992. A study on the 'runaway greenhouse effect' with a one-dimensional radiative-convective equilibrium model. J. Atmos. Sci. 49, 2256–2266.

Ohtani, E., Suzuki, A., Kato, T., 1998. Flotation of olivine and diamond in mantle melt at high pressure: implications for fractionation in the deep mantle and ultradeep origin of diamond. Washington DC American Geophysical Union Geophysical Monograph Series 101, 227–239.
Palumbo, A.M., Head, J.W., 2018. Impact cratering as a cause of climate change, surface alteration, and resurfacing during the early history of Mars. Meteorit. Planet. Sci. 53 (4), 687–725.
Palumbo, A.M., Head, J.W., Wordsworth, R.D., 2018. Late Noachian icy highlands climate model: exploring the possibility of transient melting and fluvial/lacustrine activity through peak annual and seasonal temperatures. Icarus 300, 261–286.
Perrin, M.Y., Hartmann, J.M., 1989. Temperature-dependent measurements and modeling of absorption by CO_2-N_2 mixtures in the far line-wings of the 4.3-micron CO_2 band. J. Quant. Spectrosc. Radiat. Transf. 42, 311–317.
Pierrehumbert, R.T., 1995. Thermostats, radiator fins, and the local runaway greenhouse. J. Atmos. Sci. 52, 1784–1806.
Piqueux, S., Christensen, P.R., 2009. A model of thermal conductivity for planetary soils: 1. Theory for unconsolidated soils. J. Geophys. Res. Planets 114, E09005.
Pollack, J.B., Dalton, J., Grinspoon, D., Wattson, R.B., Freedman, R., Crisp, D., Allen, D.A., Bezard, B., DeBergh, C., Giver, L.P., Ma, Q., Tipping, R., 1993. Near-infrared light from Venus' nightside: a spectroscopic analysis. Icarus 103 (1), 1–42.
Poulet, F., Bibring, J.-P., Mustard, J.F., Gendrin, A., Mangold, N., Langevin, Y., Arvidson, R.E., Gondet, B., Gomez, C., 2005. Phyllosilicates on Mars and implications for early martian climate. Nature 438, 623–627.
Pruppacher, H., Klett, J., 1996. Microphysics of Clouds and Precipitation. Atmospheric and Oceanographic Sciences Library Springer Netherlands.
Quantin-Nataf, C., Craddock, R.A., Dubuffet, F., Lozac'h, L., Martinot, M., 2019. Decline of crater obliteration rates during early martian history. Icarus 317, 427–433.
Ramirez, R.M., Kaltenegger, L., 2017, Mar, Mar. A volcanic hydrogen habitable zone. The Astrophysical Journal Letters 837, L4.
Ramirez, R.M., Kaltenegger, L., 2018. A methane extension to the classical habitable zone. Astrophys. J. 858 (2), 72.
Ramirez, R.M., Kasting, J.F., 2017. Could cirrus clouds have warmed early Mars? Icarus 281, 248–261.
Ramirez, R.M., Kopparapu, R., Zugger, M.E., Robinson, T.D., Freedman, R., Kasting, J.F., 2014. Warming early Mars with CO_2 and H_2. Nat. Geosci. 7, 59–63.
Ramirez, R.M., Kopparapu, R.K., Lindner, V., Kasting, J.F., 2014. Can increased atmospheric CO_2 levels trigger a runaway greenhouse? Astrobiology 14, 714–731.
Reese, C.C., Solomatov, V.S., 2006. Fluid dynamics of local martian magma oceans. Icarus 184, 102–120.
Reese, C.C., Solomatov, V.S., Orth, C.P., 2007. Mechanisms for cessation of magmatic resurfacing on Venus. J. Geophys. Res. Planets 112, E04S04.
Roberts, J.H., Arkani-Hamed, J., 2014. Impact heating and coupled core cooling and mantle dynamics on Mars. J. Geophys. Res. Planets 119, 729–744.
Roberts, J.H., Lillis, R.J., Manga, M., 2009. Giant impacts on early Mars and the cessation of the martian dynamo. J. Geophys. Res. Planets 114, E04009.
Rosenberg, E.N., Palumbo, A.M., Cassanelli, J.P., Head, J.W., Weiss, D.K., 2019. The volume of water required to carve the martian valley networks: improved constraints using updated methods. Icarus 317, 379–387.
Rossow, W.B., 1978. Cloud microphysics - analysis of the clouds of Earth, Venus, Mars, and Jupiter. Icarus 36, 1–50.
Rothman, L.S., Gordon, I.E., Babikov, Y., Barbe, A., Chris Benner, D., Bernath, P.F., Birk, M., Bizzocchi, L., Boudon, V., Brown, L.R., Campargue, A., Chance, K., Cohen, E.A., Coudert, L.H., Devi, V.M., Drouin, B.J., Fayt, A., Flaud, J.-M., Gamache, R.R., Harrison, J.J., Hartmann, J.-M., Hill, C., Hodges, J.T., Jacquemart, D., Jolly, A., Lamouroux, J., Le Roy, R.J., Li, G., Long, D.A., Lyulin, O.M., Mackie, C.J., Massie, S.T., Mikhailenko, S., Naumenko, O.V., Nikitin, A.V., Orphal, J., Perevalov, V., Perrin, A., Polovtseva, E.R., Richard, C., Smith, M.A.H., Starikova, E., Sung, K., Tashkun, S., Tennyson, J., Toon, G.C., Tyuterev, V.G., Wagner, G., 2013. The HITRAN2012 molecular spectroscopic database. J. Quant. Spectrosc. Radiat. Transf. 130, 4–50.
Ruedas, T., Breuer, D., 2017. On the relative importance of thermal and chemical buoyancy in regular and impact-induced melting in a Mars-like planet. J. Geophys. Res. Planets 122, 1554–1579.
Ruedas, T., Breuer, D., 2018. "Isocrater" impacts: conditions and mantle dynamical responses for different impactor types. Icarus 306, 94–115.
Ruedas, T., Breuer, D., 2019. Dynamical effects of multiple impacts: large impacts on a Mars-like planet. Phys. Earth Planet. In. 287, 76–92.
Schaake, J.C., Koren, V.I., Duan, Q.-Y., Mitchell, K., Chen, F., 1996. Simple water balance model for estimating runoff at different spatial and temporal scales. J. Geophys. Res.-Atmos. 101, 7461–7475.
Segura, T.L., McKay, C.P., Toon, O.B., 2012. An impact-induced, stable, runaway climate on Mars. Icarus 220, 144–148.
Segura, T.L., Toon, O.B., Colaprete, A., 2008. Modeling the environmental effects of moderate-sized impacts on Mars. J. Geophys. Res. Planets 113 (E12), E11007.
Segura, T.L., Toon, O.B., Colaprete, A., Zahnle, K., 2002. Environmental effects of large impacts on Mars. Science 298, 1977–1980.
Shuvalov, V., 2009. Atmospheric erosion induced by oblique impacts. Meteorit. Planet. Sci. 44, 1095–1105.
Shuvalov, V., Kührt, E., de Niem, D., Wünnemann, K., 2014. Impact induced erosion of hot and dense atmospheres. Planet. Space Sci. 98, 120–127.
Smith, D.E., Zuber, M.T., 17, coauthors, 1999. The global topography of Mars and implication for surface evolution. Science 284, 1495–1503.
Smith, D.E., Zuber, M.T., Frey, H.V., Garvin, J.B., Head, J.W., Muhleman, D.O., Pettengill, G.H., Phillips, R.J., Solomon, S.C., Zwally, H.J., Banerdt, W.B., Duxbury, T.C., Golombek, M.P., Lemoine, F.G., Neumann, G.A., Rowlands, D.D., Aharonson, O., Ford, P.G., Ivanov, A.B., Johnson, C.L., McGovern, P.J., Abshire, J.B., Afzal, R.S., Sun, X., 2001. Mars orbiter Laser Altimeter: Experiment Summary After the First Year of Global Mapping of Mars. In: 106. pp. 23689–23722.
Solomatov, V., 2015. Magma Oceans and Primordial Mantle Differentiation. pp. 81–104.
Steakley, K., Murphy, J., Kahre, M., Haberle, R., Kling, A., 2019. Testing the impact heating hypothesis for early Mars with a 3-D global climate model. Icarus 330, 169–188.
Steakley, K.E., Kahre, M.A., Murphy, J.R., Haberle, R.M., Kling, A.M., 2018. Post-impact climates on early Mars: revisiting 1-D scenarios with a 3-D GCM. In: Lunar and Planetary Science Conference. Lunar and Planetary Inst. Technical Report. vol.49. pp. 2702.
Stefani, S., Piccioni, G., Snels, M., Grassi, D., Adriani, A., 2013. Experimental CO_2 absorption coefficients at high pressure and high temperature. J. Quant. Spectrosc. Radiat. Transfer 117, 21–28.
Sung, K., Brown, L.R., Toth, R.A., Crawford, T.J., 2009. Fourier transform infrared spectroscopy measurements of H_2O-broadened half-widths of CO_2 at 4.3 μm. Can. J. Phys. 87, 469–484.
Svetsov, V.V., Shuvalov, V.V., 2015. Water delivery to the Moon by asteroidal and cometary impacts. Planet. Space Sci. 117, 444–452.
Tackley, P.J., 1996. On the ability of phase transitions and viscosity layering to induce long wavelength heterogeneity in the mantle. Geophys. Res. Lett. 23, 1985–1988.
Tackley, P.J., 2008. Modelling compressible mantle convection with large viscosity contrasts in a three-dimensional spherical shell using the yin-yang grid. Phys. Earth Planet. Inter. 171, 7–18.
Toon, O.B., Segura, T., Zahnle, K., 2010. The formation of martian river valleys by impacts. Annu. Rev. Earth Planet. Sci. 38, 303–322.
Tran, H., Boulet, C., Stefani, S., Snels, M., Piccioni, G., 2011. Measurements and modelling of high pressure pure CO_2 spectra from 750 to 8500 cm^{-1}. I - central and wing regions of the allowed vibrational bands. J. Quant. Spectrosc. Radiat. Transf. 112, 925–936.
Tran, H., Turbet, M., Chelin, P., Landsheere, X., 2018. Measurements and modeling of absorption by CO_2 + H_2O mixtures in the spectral region beyond the CO_2 ν_3-band head. Icarus 306, 116–121.
Tran, H., Turbet, M., Hanoufa, S., Landsheere, X., Chelin, P., Ma, Q., Hartmann, J.M., 2019. The CO_2-broadened H_2O Continuum in the 100–1500 cm^{-1} Region. Measurements, Predictions and Empirical Model. submitted to JQSRT.
Turbet, M., 2018. Habitability of Planets Using Numerical Climate Models. Application to Extrasolar Planets and Early Mars. Theses. Sorbonne Université/Université Pierre et Marie Curie - Paris VI.
Turbet, M., Forget, F., Head, J.W., Wordsworth, R., 2017. 3D modelling of the climatic impact of outflow channel formation events on early Mars. Icarus 288, 10–36.
Turbet, M., Tran, H., 2017. Comment on "radiative transfer in CO_2-rich atmospheres: 1. Collisional line mixing implies a colder early mars". Journal of Geophysical Research: Planets 122 (11), 2362–2365 2017JE005373.
Turbet, M., Tran, H., Hartmann, J.-M., Forget, F., 2017. Toward a more accurate spectroscopy of CO_2/H_2O-rich atmospheres: implications for the early martian atmosphere. LPI Contributions 2014, 3063.
Turbet, M., Tran, H., Pirali, O., Forget, F., Boulet, C., Hartmann, J.-M., 2019. Far infrared measurements of absorptions by CH_4 + CO_2 and H_2 + CO_2 mixtures and implications for greenhouse warming on early Mars. Icarus 321, 189–199.
Urata, R.A., Toon, O.B., 2013. Simulations of the martian hydrologic cycle with a general circulation model: implications for the ancient martian climate. Icarus 226, 229–250.
Vaughan, W.M., Head, J.W., 2014. Impact melt differentiation in the South Pole-Aitken basin: some observations and speculations. Planet. Space Sci. 91, 101–106.
Vaughan, W.M., Head, J.W., Wilson, L., Hess, P.C., 2013. Geology and petrology of enormous volumes of impact melt on the Moon: a case study of the Orientale basin impact melt sea. Icarus 223, 749–765.
Vickery, A.M., 1990. Impacts and atmospheric erosion on the early Earth. In: Meteorite Impact on the Early Earth. LPI Contributions. vol.746. pp. 51.
Wang, F., Cheruy, F., Dufresne, J.-L., 2016. The improvement of soil thermodynamics and its effects on land surface meteorology in the IPSL climate model. Geosci. Model Dev. 9, 363–381.
Werner, S.C., 2008. The early martian evolution - constraints from basin formation ages. Icarus 195, 45–60.
Werner, S.C., 2014. Moon, Mars, Mercury: basin formation ages and implications for the maximum surface age and the migration of gaseous planets. Earth Planet. Sci. Lett. 400, 54–65.
Williams, R.M.E., Grotzinger, J.P., Dietrich, W.E., Gupta, S., Sumner, D.Y., Wiens, R.C., Mangold, N., Malin, M.C., Edgett, K.S., Maurice, S., 2013. Martian fluvial conglomerates at Gale crater. et al.. Science 340, 1068–1072.
Wood, E.F., Lettenmaier, D.P., Zartarian, V.G., 1992. A land-surface hydrology parameterization with subgrid variability for general circulation models. J. Geophys. Res.-Atmos. 97, 2717–2728.
Wordsworth, R., Forget, F., Eymet, V., 2010. Infrared collision-induced and far-line absorption in dense CO_2 atmospheres. Icarus 210, 992–997.
Wordsworth, R., Forget, F., Millour, E., Head, J.W., Madeleine, J.-B., Charnay, B., 2013. Global modelling of the early martian climate under a denser CO_2 atmosphere: water cycle and ice evolution. Icarus 222, 1–19.
Wordsworth, R., Kalugina, Y., Lokshtanov, S., Vigasin, A., Ehlmann, B., Head, J., Sanders, C., Wang, H., 2017. Transient reducing greenhouse warming on early Mars. Geophys. Res. Lett. 44, 665–671.
Wordsworth, R.D., 2016. The climate of early Mars. Annu. Rev. Earth Planet. Sci. 44, 381–408.
Wordsworth, R.D., Kerber, L., Pierrehumbert, R.T., Forget, F., Head, J.W., 2015. Comparison of "warm and wet" and "cold and icy" scenarios for early Mars in a 3-D climate model. J. Geophys. Res. Planets 120, 1201–1219.
Xie, S., Tackley, P.J., 2004. Evolution of helium and argon isotopes in a convecting mantle. Phys. Earth Planet. Inter. 146, 417–439.